The effects of swirl vanes and a vortex stabilizer on the dynamic flow field in a cyclonic separator

Gustavo E.O. Celis [b], Juliana B.R. Loureiro [a,b,*], Paulo L.C. Lage [a,c], Atila P. Silva Freire [a,b]

[a] *Interdisciplinary Center for Fluid Dynamics (NIDF/UFRJ), R. Moniz Aragão 360, 21941-594 Rio de Janeiro, Brazil*
[b] *Programa de Engenharia Mecanica (PEM/COPPE/UFRJ), C.P. 68503, 21941-972 Rio de Janeiro, Brazil*
[c] *Programa de Engenharia Quimica, Universidade Federal do Rio de Janeiro, (COPPE/UFRJ), Brazil*

HIGHLIGHTS

- Effects of two internal components of a particular gas–liquid cyclonic separator are studied.
- Internal elements have an important influence on the position of the center of rotation.
- Mean velocity and the precession of the vortex core (PVC) are measured through PIV.
- The two internal components stabilize the precessing vortex core
- Assessment of the PVC frequency of a confined swirling flow for low frequency 2D-PIV data.

ARTICLE INFO

ABSTRACT

The present work describes the isolated and combined effects of two internal components – swirl vanes and a vortex stabilizer – on the properties of the flow inside a particular type of gas–liquid cyclonic separator. These elements play an important role in the optimization of the catch efficiency of the gas and liquid phases but may otherwise result in a large increase in pressure drop. It is shown that the vanes and the vortex stabilizer have a considerable influence on the position of the center of rotation of the flow, which clearly does not coincide with the geometric center of the cyclone. Here, an experimental study investigates the velocity field and the resulting pressure drop inside the cyclone to account for the individual effects caused by the two internal components. Particle Image Velocimetry is used to characterize the mean velocity field and the precession of the vortex core (PVC). For the different geometrical configurations discussed in the present work, the influence of the swirl vanes was always beneficial to reduce the residence time and thus decrease the pressure drop across the cyclonic separator. The present work also introduces a method for the assessment of the PVC frequency of a confined swirling flow for low frequency 2D-PIV measurements.

© 2021 Elsevier Ltd. All rights reserved.

1. Introduction

The separation of bubbles, drops or particles from a multiphase flow stream is a ubiquitous problem in industrial applications. In view of the ever growing rules on worldwide environmental protection, industries may be severely exposed to financial penalties on such common events as the discharge of contaminated water or flared gas. From this standpoint, there exists an urgent need for the development of very efficient in-line separation technology.

A second constraint often encountered in applications is the limited room in which separators must be installed. Since these devices frequently need to be fitted to existing facilities, size is commonly a great concern. A typical example is provided by the oil industry. As the life of a production well increases, an ever greater cut of water is normally produced, which needs to be separated and discarded. Any installed primary separation system is then increasingly demanded, implying that upgrades need to be implemented many times.

Most often, large vessels are used as gravity separators. The difficulty is that the size and weight of these separators demand high costs and large spaces in processing facilities, especially on offshore structures. Gravity-driven separation implies time-consuming processes and limited production targets. The recent trend is that these vessels are progressively replaced by compact separation systems assembled from inclined pipes (junction flows),

Gustavo E.O. Celis, Juliana B.R. Loureiro, Paulo L.C. Lage et al.

Chemical Engineering Science 248 (2022) 117099

Nomenclature

b	Swirling blades height [mm]	Eu	Euler number
c	Vertical blades length [mm]	Re	Reynolds number
e	Cone base length [mm]	Sg	Geometrical swirl number
f	Closing cone height [mm]	U_{in}	Inlet mean velocity $[\mathrm{ms^{-1}}]$
g	Baffles height [mm]	V_r	Radial mean velocity $[\mathrm{ms^{-1}}]$
h	Vortex finder length [mm]	V_t	Tangential mean velocity $[\mathrm{ms^{-1}}]$
l	Characteristic cyclone length [mm]	V_z	Axial mean velocity $[\mathrm{ms^{-1}}]$
m	Gap between baffles [mm]	Q_g	Gas flow rate $[\mathrm{m^3h^{-1}}]$
r	Radial distance [mm]	d_b	Baffles diameter [mm]
z	Axial distance [mm]	d_{in}	Inlet diameter [mm]
A	Configuration without internals	d_{vf}	Vortex finder diameter [mm]
B	Configuration with Chinese hat element	t	Time [s]
C	Configuration with swirl vanes element	f_{pvc}	PVC frequency $[\mathrm{s^{-1}}]$
D	Configuration with all elements	$\overline{x}_c, \overline{y}_c$	Vortex core center position [mm]
D	Cyclone diameter [mm]	ρ	Density $[\mathrm{kg\,m^{-3}}]$
H	Total height of cyclone [mm]	μ	Viscosity $[\mathrm{m^2s}]$
L	Height of the Chinese hat element [mm]	ζ	Dummy variable
R	Cyclone radius [mm]	β	Vortex core rotation angle [rad]
St	Stokes number	β_{pred}	Assessment angle [rad]
X, Y	Cartesian coordinate system	ϕ	Normalized parameter
Y'	Relative coordinate		
Ds	Displacement magnitude [mm]	**Subscripts**	
ΔP	Pressure drop	f	Fluid
PD	Percentage deviation	p	Particle
Std	Standard deviation		
CV	Variation coefficient		

swirl pipes, cyclones or their combination (Kremleva et al., 2010; Austrheim et al., 2008). The advantages of cyclonic separators are their low cost and weight, no moving parts, low pressure drop, low maintenance, simple installation and operation. As cyclones can deal with large flow rates and small residence times, production can be increased proportionately to the separation capacity.

An important feature for the design of cyclones aimed at the oil industry is the requirement that they should be capable of accounting for large changes in the flow rates and phase fractions throughout the operational life of a well. All geometrical parameters must then be specified so that separators are able to provide optimum separation efficiency across a large interval of operational conditions.

Important geometrical parameters for the design of a reverse flow cyclone separator include (i) the inlet area and angle, (ii) single or double inlet arrangements, (iii) the relation between the main body diameter and its length, (iv) vortex finder diameter and length and (v) cone angle (in case a conic section is used). A successful design is judged on some performance parameters, such as the separation efficiency and the pressure drop. Unfortunately, the very complex flow inside a cyclone separator implies that correctly predicting its performance is not a simple task. The inlet fluid mixtures may be difficult to characterize and small changes in the geometry of the inlet, main body, or internal components, can have a significant impact on the local flow field and turbulence levels, which, in turn, affect the pressure drop and the separation efficiency. Despite the vast literature on this subject, few papers provide a comprehensive experimental characterization of the mean and turbulent velocity fields inside cyclone separators with internal components.

The purpose of the present work is to investigate the flow dynamics and pressure drop for a reverse flow cylindrical cyclone with two elements (Fig. 1): a swirl blade section and a conical bottom plate. Four distinct geometric configurations are studied for three different inlet flow conditions. The four configurations permit the isolated effects of the internals to be independently assessed, clearly revealing their particular advantages and drawbacks and how their combinations can be beneficial to flow phase separation.

Particle Image Velocimetry (PIV) is used to assess the mean velocity fields in the phase separation region. One key element to the present investigation is the determination of the center of flow rotation. Through PIV, this can be made in two ways: (i) all the instantaneous velocity fields are averaged so that the averaged center of rotation can be evaluated from the mean velocity fields, or (ii) the center of rotation of every instantaneous velocity field is calculated and the averaged value is then evaluated. Here, both procedures are carried out and compared. The latter approach permits the assessment of the precession frequency of the vortex core.

The evaluation of the center of rotation of the flow is not a simple matter for PIV measurements and for this reason the discussion is detailed in an appendix. On swirling flows the seeding particles often skip the center of the vortex core, creating a region of particle-lacking area (PLA) that increases as the swirl intensity increases.

The cyclone investigated in the present work is illustrated in Fig. 1. This equipment is frequently used in processing plants where gas demisting is required under conditions of high gas flow rates and high liquid removal efficiency (98 to 99%). In addition to these two features, the equipment is very compact, has a high turn-down ratio (factor of 3), is suitable for services with slightly fouling and can handle slug flows. The gas–liquid mixture enters the cylindrical body through a tangential inlet, which imposes flow rotation around the vortex finder. The helical blades of the swirl section direct the flow downwards. The vanes increase the axial velocity component, reduce the residence time and favor a decrease in pressure drop. This section, however, decreases the tangential velocity component and normally the separation efficiency. The
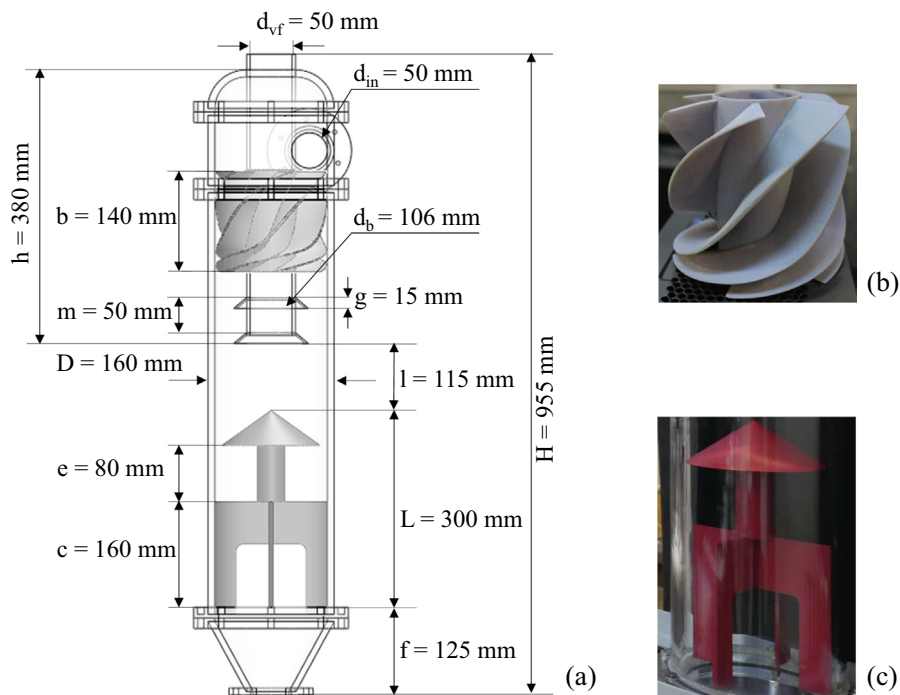
Fig. 1. Reverse flow cyclone with internals. Cyclone geometry: a) relevant geometrical parameters and photographs of the b) swirl blades and c) Chinese hat (conical plate). l = (115 mm) is a fixed length, which does not change in the absence of the Chinese hat.

vortex finder is fitted externally with two thin conical baffles to minimize liquid drop carry over. The baffles also reduce any short-cut flows connecting the tangential inlet flow to the gas outlet flow. The swirl effect directs the denser fluid to the cylindrical wall and onto the lower portion of the separator toward the liquid outlet. The separated gas reverses direction and flows upwards through the center part of cyclone to the vortex finder.

The conical plate element (*Chinese hat*) is illustrated in Fig. 1. The Chinese hat reduces the contact between the gas vortex core and the liquid phase; its diameter is slightly shorter than the internal diameter of the cylinder, so that the falling liquid film on the vertical wall can flow downstream undisturbed. The liquid level is typically maintained midway through the height of four supporting legs. The legs are such arranged as to break the swirl motion of the liquid as it flows downwards, acting as a counter-rotation element. The primary role of the Chinese hat is to stabilize the flow and prevent separated liquid from returning to the main gas stream.

Single-phase flow experiments were performed for a first assessment of the influence of the swirl blades and the Chinese hat on the velocity field and pressure drop across the cyclone separator. The swirl vanes increase the axial velocity, reduce the residence time and the global pressure drop. For the different configurations investigated, the influence of the rotation section is shown to be consistently beneficial.

2. Brief literature review

Tangential inlet and vanes have not often been used in industry to promote centrifugal phase separation (gas–liquid and liquid–liquid). The main advantage resulting from their combination – as shown in Fig. 1 – is a substantial reduction in the pressure drop across the separator.

The present brief literature review aims at illustrating some of the typical features of cyclones with tangential inlet, their experimental characterization, recent improvements (inlet angle, vortex

finder design) and numerical simulation. Alternative concepts for centrifugal phase separation have been introduced in literature with a view to reduce space and offer different flow inlet options, but these are not the subject of the present work. For example, tubes fitted with internal vanes have been optimized over the last few years to be used in the phase separation of liquid–liquid, gas–liquid and gas–solid mixtures.

The early works, in general, to study the flow inside a cyclone resorted to Pitot tubes and flow visualization techniques based on smoke and stroboscopic light (Ter Linden, 1949; Smith, 1962). Since the nineties, non-intrusive techniques such as Laser-Doppler Velocimetry (LDV) and Particle Image Velocimetry (PIV) started to be used (Monredon et al., 1992; Peng et al., 2001; Bergström and Vomhoff, 2007).

Van Campen and co-workers (van Campen et al., 2012) performed experiments (LDA and electrical conductivity) and numerical simulations (RSM-SSG) in a tube with an axial swirl element to assess the overall efficiency of the separator. The experimental characterization of the flow in in-line separators is difficult since the process occurs in a very short time and conventional multiphase sensors typically do not work properly under this condition. Sahovic and collaborators (Sahovic et al., 2020) proposed an innovative concept to control in-line fluid separation through electrical tomography and wire-mesh sensors, fast and massive data processing and appropriate process control strategy. Flow in tubes with a tangential inlet was numerically studied (LES simulations) by Derksen (Derksen, 2005) with a view to investigate evading flow features including vortex breakdown, laminarization of the vortex core and the extreme sensitivity of the mean velocity profiles in the tube to the exit pipe diameter.

The combination of a tangential inlet and vanes was investigated by Zhou and collaborators (Zhou et al., 2018). The geometry studied in this work is similar to the present one, but not often discussed in literature. Experiments and numerical simulations were performed for four distinct configurations. The vanes were shown to considerably influence the flow features. The study suggests that

Gustavo E.O. Celis, Juliana B.R. Loureiro, Paulo L.C. Lage et al.

Chemical Engineering Science 248 (2022) 117099

there exists a critical value for the number of spirals below or above which there is a marked increase in collection efficiency, pressure drop and tangential velocity.

Some previous contributions particularly discussed the present geometry (Nanninga et al., 2001; Janssen and Betting, 2006). These studies, however, were mainly concerned with catch efficiency and pressure losses and no results on local parameters were presented.

The influence of the vortex finder diameter on the flow field inside a reverse flow gas cyclone separator was investigated by Hoekstra and co-workers Hoekstra et al. (1999). Experimental data obtained through laser-Doppler anemometry were used to validate RANS numerical predictions. The $\kappa - \epsilon$ and RNG-$\kappa - \epsilon$ models were considered unsuitable for a good prediction of cyclonic flows, as unrealistic axial and tangential velocity distributions were obtained. Predictions provided through RSM-models furnished a better agreement with the experimental data. The work showed that a decrease in the vortex finder diameter reduced the vortex core size and increased the maximum tangential velocity. The influence of a vortex stabilizer, positioned at the base of the cyclone, was also investigated by the authors. The stabilizer reduces re-entrainment of particles from the collection hopper and inhibits axial flow reversal near the cyclone axis. The authors mention that this effect is limited to the flow in the lower region of the separation zone. This vortex stabilizer has the same purpose of the Chinese hat investigated in the present work, but with a different geometry.

A new design of vortex finder with a view to increase efficiency and reduce pressure drop in a swirl tube separator was investigated by Li and collaborators Li et al. (2015). The studied vortex finder was conical and slotted off the side wall. The velocity field was measured through a Pitot tube. The authors mention that the slotted vortex finder acts as a pre-separation step, increasing the particle collection efficiency and reducing the pressure drop by 30%. As explained, a portion of the fluid enters through the slots, thus reducing the occurrence of short circuit of particles from the entrance to the vortex finder and, as the fluid velocity decreases, the pressure drop follows the same trend.

An experimental study of gas–liquid flows inside tangential inlet cylinder cyclones was conducted by Bandyopadhyay and Gad-el Hak (1996). The work focused on the sensitivity of the gas-core configurations to two parameters: i) the relative angle between the tangential inlet and the outlet and ii) the ratio of length to diameter of the cylinder. Using flow visualization, the work identified eight types of core patterns, which were classified between two basic modes: straight and helical-spiral. The authors presented a kinematic model to explain the observed changes in the vortex core. The effects of liquid flow rate variation and drop diameter at the entrance were also studied.

Focusing on the role of the internals, Austrheim and co-workers Austrheim et al. (2008) discussed possible improvements in the design of gas scrubbers, which are typically used for large gas to liquid ratios. The investigated configurations consisted of different types of separation equipment arranged in series. The influence of a vane-type inlet, a mist mat and a cyclone deck were investigated. Experiments were conducted for gas–liquid inlet flows, using water and oil as the liquid phase. The work also discussed an empirically quantified factor known as the Sounders-Brown value. The flow velocity field was not investigated.

Despite the great deal of information that can be obtained through global flow field characterization, few works in literature used PIV to investigate swirling flows inside cyclones. Stereoscopic PIV was used by Liu and co-authors Liu et al. (2006) to study the cylindrical and conical separation zones as well as the dust hopper area. The authors concluded that the inlet gas velocity does not exert a significant impact on the flow patterns in the cyclone. Results indicate that separated particles may eventually be re-

entrained into the cyclone from the dust bin degrading its separation efficiency.

The limitations of numerical simulations to investigate and provide answers to complex industrial cyclonic flows are discussed in Derksen and Van den Akker (2000). In particular, for moderate and large Reynolds numbers, the broadband spectra of turbulence means that the length and time scales cannot be numerically fully resolved, so that some expected flow information may be difficult to obtain. Derksen and Van den Akker (2000) resorted to large eddy simulation (LES) and a lattice-Boltzmann discretization of the Navier–Stokes equation to investigate *single phase* flow inside a reverse-flow cylinder cyclone. By doing this, the authors managed to achieve sufficiently high spatial and temporal resolution to adequately resolve the precession of the vortex core phenomena. Numerical results were compared with the experimental data of Hoekstra and co-workers Hoekstra et al. (1999). The authors observed a short-cut flow from the inlet to the vortex finder.

The influence of the inlet angle on the flow pattern and on the pressure drop was investigated by Misiulia and co-authors Misiulia et al. (2015) through LES with closure provided by the dynamic Smagorinsky-Lilly subgrid-scale model. The inlet angles varied between 7 and 25°. Cyclones with helical-roof inlets were compared with tangential-inlets cyclones. The authors concluded that increasing the inlet angle reduces the axial velocity and increases the maximum radial velocity under the vortex finder. This effect shows a negative impact on the overall collection efficiency. The differences in geometry of the ten investigated cyclones were characterized by means of the geometrical swirl number, which expresses a measure of the ratio of the tangential to axial momentum.

RANS-RSM was used to simulate the gas flow fields inside cyclones with different inlet section angles (Qian and Zhang, 2007). The authors discussed the intricate relations between the inlet angle and the pressure drop, the tangential velocity field and the separation performance of the cyclone. In particular, the authors varied the vortex finder depth to investigate the influence of the inlet angle and the short-cut flow from the entrance to the vortex finder. The separation efficiency was shown to be influenced not only by the inlet angle but also by the vortex finder diameter and depth. The work showed that an inlet angle of 45° decreases the pressure drop up to 30%.

The swirl flow inside a cylinder cyclone was investigated by Hreiz and collaborators (Hreiz et al., 2011) through commercially available computational fluid dynamics codes. The work compares the performance of RANS simulations with LES and their limitations. The authors showed that for a single inlet separator the realizable $\kappa - \epsilon$ model furnished the best results for predictions of the velocity profiles. The level of turbulent kinetic energy was underestimated by both LES and RANS simulations. The work showed that a rectangular inlet reduces the vortex warping and increases the angular momentum in comparison to a circular inlet.

No study was found in the literature which provided *local* experimental or numerical data for the specific geometry of cyclone investigated in the present work.

3. Experiments

3.1. Experimental apparatus

The experimental apparatus was designed to operate with either single or two-phase gas–liquid flows. In the present study, the primary objective is to characterize the single phase flow dynamics inside the cyclone shown in Fig. 1 through optical techniques. For this reason, only single phase flow experiments were carried on.

Gustavo E.O. Celis, Juliana B.R. Loureiro, Paulo L.C. Lage et al.

Chemical Engineering Science 248 (2022) 117099

A diagram of the test bench is shown in Fig. 2. The air-compressor is equipped with a drying and storage system and is set to work at a pressure of 10 bar, which is enough to supply a maximum flow rate of 150 m^{3}h^{-1} at standard conditions. A calibrated pressure transducer and a calibrated vortex flow meter allow the measurement of the air flow rate at the entrance line of the separator with an overall uncertainty of 4% of the reading.

For the PIV measurements, the tracer particles are injected in the flow through an atomizer manufactured by the Spraying System Company. Compressed air is used to actuate the atomizer and keep the tiny generated particles in suspension. A mixing chamber (see Fig. 2) is directly connected to the inlet pipe to blend the suspended particles with the main stream and retain, by gravity effects, the largest drops.

Pressure taps are fitted to the gas inlet and outlet pipes to measure the overall pressure drop in the cyclone. The differential pressure transducer is a calibrated Endress-Hauser equipment, model PMD75. Calibration was performed by comparing the digitized pressure signal with results provided by a reference water column manometer. The calibration curve showed a linear behavior and the maximum overall uncertainty was lower than 0.6% of the reading. The locations of the pressure taps are shown in Fig. 3. Four pressure taps are symmetrically distributed at a same cross plane on the top of the vortex finder. They are used to assess the average radial pressure gradient value of the swirling flow. In the inlet pipe flow, just one pressure tap is used. In the present investigation, the gas outlet remains open to the atmosphere and the liquid outlet is shut.

3.2. Cyclone geometry and tested configurations

The prototype of the separator was made of acrylic as to permit the use of non-intrusive optical measurement techniques. Most of the dimensions of the separator are shown in Fig. 1. The main geometrical details are discussed next.

The separator has a 50 mm ID tangential inlet (d_{in}) that is directly connected to the inlet pipe shown in Fig. 2. The vortex finder has the same inner diameter as the inlet pipe ($d_{vf} = d_{in}$) and is 380 mm in height. The vortex finder is externally fitted with two conical baffles, one at the inlet section and another at position $z = 50$ mm (see Fig. 1). The baffles collect and prevent the capture
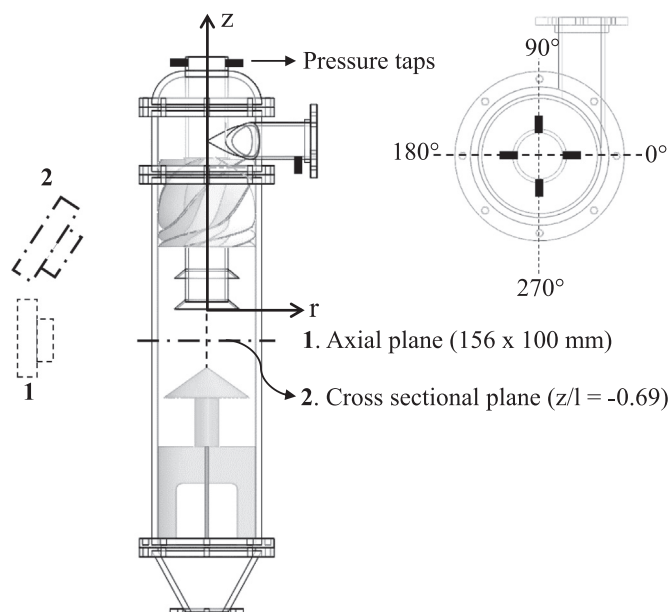

Fig. 3. Location of pressure taps, coordinate system (r,z) definition and 2D PIV set-up. Camera arrangement for measurements at 1) axial plane and 2) cross section plane.

of liquid droplets by the gas stream that flows out through the vortex finder. The cylindrical body is 795 mm long and has an internal diameter of 160 mm. The total height of the separator is 955 mm.

The two internal elements of interest are the stationary swirl vanes and the Chinese hat, illustrated separately in Fig. 1. The swirl section is mounted externally to the vortex finder and consists of 6 helical vanes with inlet and outlet angles of 30° and 20°, respectively. These values follow the design recommendations of Hoffmann and Stein (2008). The vanes are 1 mm thick in the inlet and outlet regions and 3 mm thick in the middle part of the section. The whole section was manufactured in a 3D printing machine to ensure geometrical precision. The conical section is located at the bottom part of the cyclone and is supported by four legs.
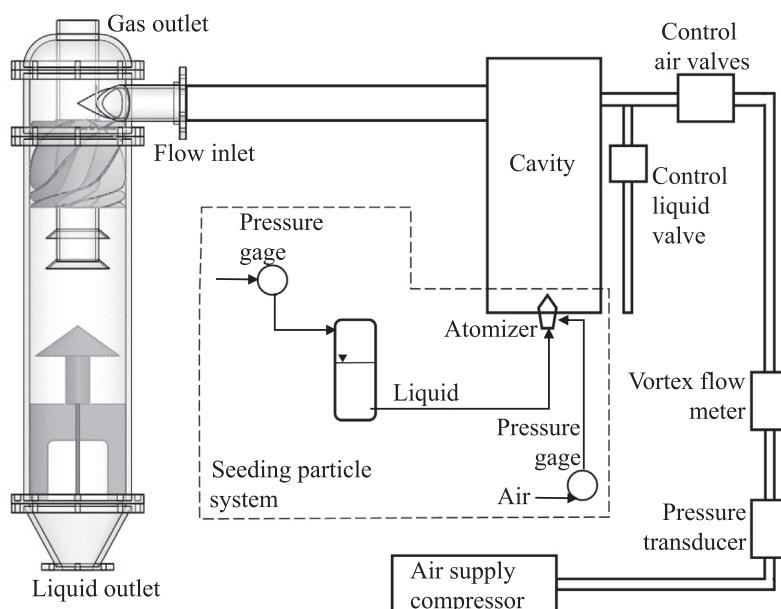

Fig. 2. Experimental set-up.

Gustavo E.O. Celis, Juliana B.R. Loureiro, Paulo L.C. Lage et al.

Chemical Engineering Science 248 (2022) 117099

The four investigated geometrical configurations are shown in Fig. 4. The tangential inlet section and the bottom conical outlet are the same for all tested cases. Configuration **A** is the simplest possible and only contains the vortex finder. The addition of the Chinese hat results in configuration **B**. The influence of the swirl blades is investigated through configuration **C**. The simultaneous effects of the two internals are discussed in configuration **D**.

The experimental conditions are listed in Table 1.

The geometric swirl number *Sg* denotes the ratio of the tangential to axial momentum (Gupta et al., 1984; Hoekstra et al., 1999) and is defined as

$$Sg = \frac{\pi d_{vf} D}{4 A_{in}}, \tag{1}$$

where A_{in} is the inlet cross section. For the current prototype, *Sg* is 3.2.

3.3. Particle Image Velocimetry

A 2D PIV system from Dantec Dynamics was used to characterize the flow field. The system illumination is provided by a Litron doubled pulsed Nd:YAG laser with a wavelength of 532 nm, pulse duration of 120 ns, energy of 200 mJ per pulse and repetition rate of 15 Hz. The beam passes through a set of cylindrical and spherical lenses, creating a light-sheet of about 1 mm of thickness. The light reflected by the tracer particles is recorded by a gray scale CCD camera with image size of 1600×1200 pixels and 8-bit resolution. The camera was fitted with a Nikkor 60 mm f/2.8D lens. System synchronization, image processing and cross-correlation were performed through the DynamicStudio Software, version 2015a.

Small particles of approximately 2 μm and specific gravity of 1.001 were generated by atomization of a 2.5 % wt sugar solution. The main criterion to make sure that tracer particles accurately followed the flow was based on the Stokes number (*St*), defined as

$$St = \frac{t_p}{t_f} = \frac{\left(2\rho_p + \rho_f\right)\left(\frac{d_p^2}{36\mu_f}\right)}{\frac{D}{V_t}}, \tag{2}$$

where t_p and t_f are the tracer particles and vortex field characteristic time scales, respectively; ρ_p and ρ_f are the particle and fluid den-

Table 1
Experimental flow conditions.

Conditions	Inlet temperature (K)	Inlet gas flow rate (m³h⁻¹)	Reynolds number
E1	298	34.5	14,100
E2	304	77.5	32,100
E3	302	142.0	58,400

sity, d_p is the particle diameter, μ_f is the viscosity of the fluid, *D* is the diameter of the cyclone and V_t is the tangential velocity. According to Brennen (2005), if $St < 0.1$, the particles will have the ability to follow the flow. In the present measurements, the maximum Stokes number was 0.0022.

To characterize the velocity field inside the separator, two measurement campaigns were conducted: (i) at the axial plane and (ii) at a cross section underneath the vortex finder (see Fig. 3). Please, also note the location of the pressure taps and of the coordinate system (r, z).

3.3.1. Axial plane measurements

The axial velocity component was measured at the 0° - 180° plane (Fig. 3), in a region limited by the bottom of the vortex finder and the top of the Chinese hat. This region defines a common separation area for the four configurations studied.

The laser sheet was set in a vertical orientation, that coincided with the 0° - 180° plane, to uniformly illuminate the field of view of 156×100 mm. The camera was set normal to the light-sheet. A dotted calibration target was used to minimize optical distortions near the cyclone walls.

Because of the out-of-plane tangential velocity component in swirling flows, the adjustment of the time between laser pulses needs to be carefully chosen. For the present experimental conditions (see Table 1), this parameter ranged from 5 to 90 μs.

The velocity field was computed through the Adaptive Correlation (DynamicStudio 2015a) algorithm, which uses successive intermediary results obtained from an initial interrogation area down to the smaller sizes until the final interrogation area is reached. For the present measurements, the interrogation window ranged from 64×64 pixels to 16×16 pixels. The final spatial resolu-
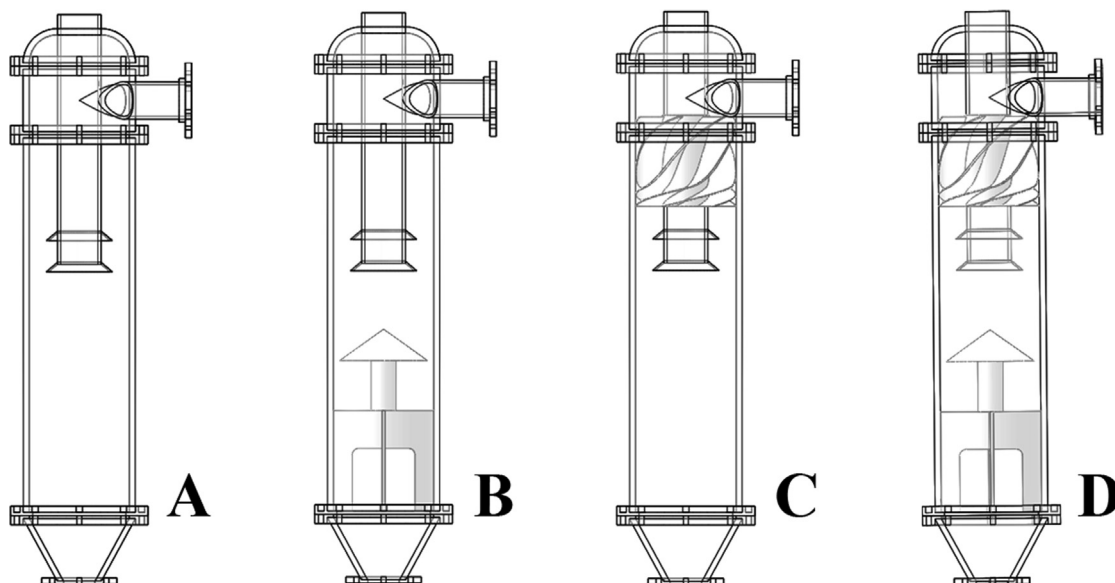

Fig. 4. The four geometrical configurations investigated: **A**, vortex finder and cylindrical body; **B**, Chinese hat; **C**, swirl vanes; **D**, complete configuration with the two internals.

Gustavo E.O. Celis, Juliana B.R. Loureiro, Paulo L.C. Lage et al.

Chemical Engineering Science 248 (2022) 117099

tion of the vector field is 0.57 mm. The overall measurement uncertainty estimated from aleatory and systematic sources reaches a maximum value of 3%.

3.3.2. Cross section plane measurements

To measure the radial and tangential velocity components the laser plane was positioned to illuminate a cross section of the cyclone body and the camera was mounted on a Scheimpflug adaptor in an off-axis position. The perspective distortion which results from this configuration was compensated and corrected through the use of a de-warping algorithm applied to the vector maps.

The measurement station was located at $z/l = -0.69$ (Fig. 3), where z denotes the vertical axis of the coordinate system and l

is the distance between the bottom of the vortex finder and the top of the Chinese hat. $l = 115$ mm is a fixed distance and it remains unaltered for the different configurations.

For this experimental campaign, a gray scale CCD camera with 1280×800 pixels and 12-bit resolution was used with a Nikkor 105 mm f/2.8D lens. The camera was positioned at an off-axis angle of 33.8°. Before each measurement, a dotted circular calibration target was positioned at the cross section measurement plane. The appropriate Scheimpflug angle was adjusted so that the whole field of view could be seen in a sharp focus. During the calibration procedure, an imaging model fit is used to describe the distortion. This built-in numerical model available in DynamicStudio (2015a) was used for image and vector map de-warping. This is done by
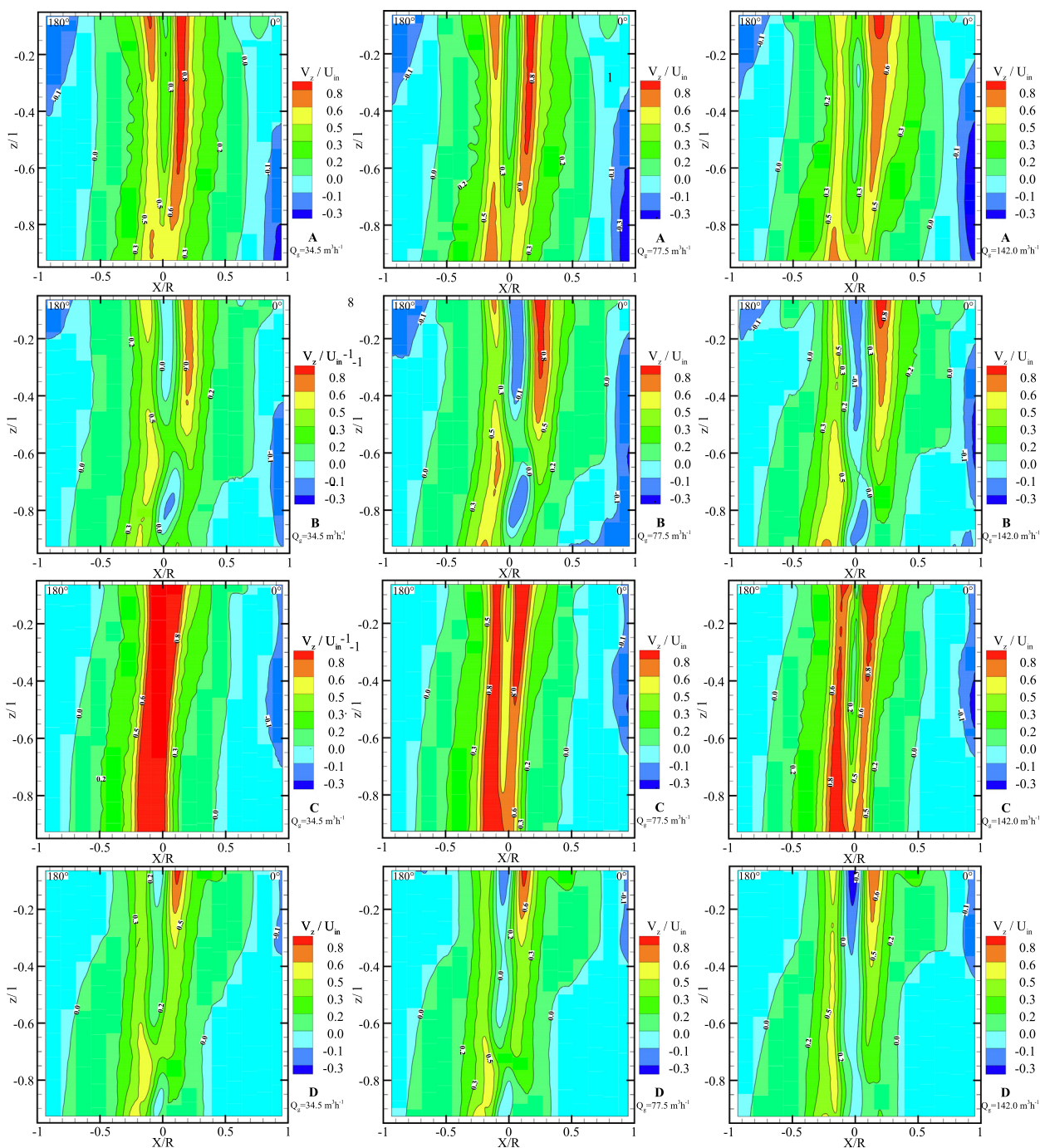

Fig. 5. PIV measured axial velocity fields (V_z) for all configuration **A** to **D** (from top to bottom) and all gas flow rates 34.5, 77.5 and 142.0 m³h⁻¹ (left to right).

Gustavo E.O. Celis, Juliana B.R. Loureiro, Paulo L.C. Lage et al.

Chemical Engineering Science 248 (2022) 117099

imposing a re-sampling grid in the lightsheet plane, so that each of the grid points in the re-sampling grid is mapped to a corresponding point in the image plane. From this calculated pixel position a grayscale value is derived from the original image and assigned to a pixel in the de-warped image.

In addition to image distortion, the flow through the light-sheet plane can severely disturb the measurement of in-plane velocities, especially if the velocity component through the plane is of the same or higher order of magnitude as the in-plane velocities. This scenario is typical of swirling flows in cyclones. However, if the axial (through-plane) velocity is known, it is possible to predict and compensate for the resulting errors in the calculated tangential and radial (in-plane) velocities (Liu et al. (2007)). This algorithm is implemented in a built-in function of DynamicStudio™ and has been used to eliminate or minimize this type of measurement error.

The field of view for the cross-sectional measurements was 191.5×187.9 mm. Post-processing images follow the same correlation used for axial measurements. The spatial resolution of the vector field maps is 0.87 mm. Time between pulses ranged from 20 to 140 μs. For the cross-section velocity measurements, the overall uncertainty estimated from random and systematic sources has a top value of 1.8% of the reading.

4. Experimental results

4.1. Velocity fields

The flow conditions 1, 2 and 3 of Table 1 were used to characterize the three velocity components (V_z, V_t and V_r) for every cyclone configuration. The dimensionless velocities are referred

Table 2
Position of flow rotation. Please see Fig. 8 for a definition of the coordinate system.

Configuration	Flow Condition	X_c [mm]	Y_c [mm]
A	E1	10.8	−6.6
	E2	1.6	−5.8
	E3	1.6	−4.7
B	E1	7.6	−4.9
	E2	5.9	−5.8
	E3	2.2	−8.7
C	E1	2.4	−4.0
	E2	−6.2	−4.1
	E3	1.9	−3.5
D	E1	−1.9	−5.8
	E2	−2.8	−5.8
	E3	−3.1	−6.2

to the inlet mean velocity U_{in}. The averaged velocity fields shown below were evaluated from 4,000 images over a sampling time interval of 4.44 min (15 Hz acquisition rate).

Fig. 5 shows for all configurations (**A** to **D**) the PIV measurements of the axial velocity fields in the plane defined in Fig. 3. The results are presented for all three gas flow rates (34.5, 77.5 and 142.0 $m^3 h^{-1}$). The differences in flow pattern as Fig. 5 is inspected from top to bottom are evident; these differences result from changes in the cyclone geometry. However, changes observed with the increase in the gas flow rate (left to right) are not much pronounced.

To all cyclone configurations, the downward free vortex and the forced upward vortex keep their general global behavior. The break in symmetry is a result of the tangential inlet, and varies significantly with all configurations, **A** to **D**. In fact, the break in symme-
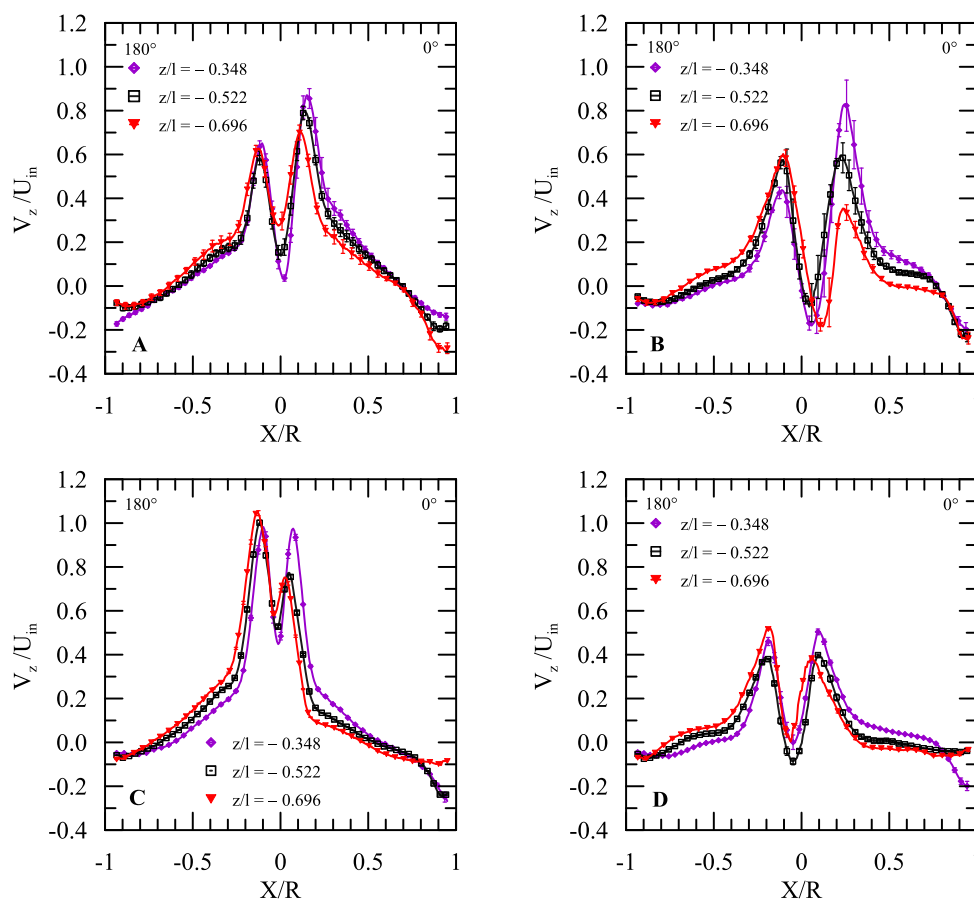

Fig. 6. Local PIV measured axial velocity fields (V_z) for all configuration **A** to **D** and flow rate 77.5 $m^3 h^{-1}$ at positions $z/l = −0.348, −0.522$ and $−0.696$.

Gustavo E.O. Celis, Juliana B.R. Loureiro, Paulo L.C. Lage et al.

Chemical Engineering Science 248 (2022) 117099

try is more apparent in the region near the Chinese hat ($z/l = -1$), with a predominance to the left (negative X/R) of higher velocities. At the vortex finder region ($z/l = 0$), the velocity field is much more symmetrical, in particular for configuration **D**, the full configuration. On the other hand, the Chinese hat stabilizes and accelerates the central vortex core (configurations **B** and **D**), creating regions of reverse (downward) flow (blue colored regions).

The velocity fields for configuration **A** show the typical flow pattern occurring in cyclonic separators. The axial mean velocity is negative close to the wall and positive in the center. The negative (downward) velocities relate to the flow that would escape through the underflow; positive velocity is related to the flow that leads through the overflow. Around the vertical axis ($X/R = 0$), two peaks of maximum velocity are observed, originating in between a region of decelerated flow (see also Hoffmann et al., 1996). Configuration **B** is characterized by two effects: the flow deceleration and the stabilization of the precessing vortex core. The flow core does not remain aligned to the geometric axis, giving origin to a coherent precessing movement of helical shape (Syred, 2006).

The swirl blades of configuration **C** organize the flow streamlines and reduce the effects of deceleration and reverse flow. As a result, the PVC phenomenon is also reduced. The highest velocity peaks occur in configuration **C** (red colored regions), meaning that most of the upward exit flow is concentrated in a narrow band of diameter about 0.1D where no negative velocities are observed. The high upward axial velocities induced by the blades in the cen-
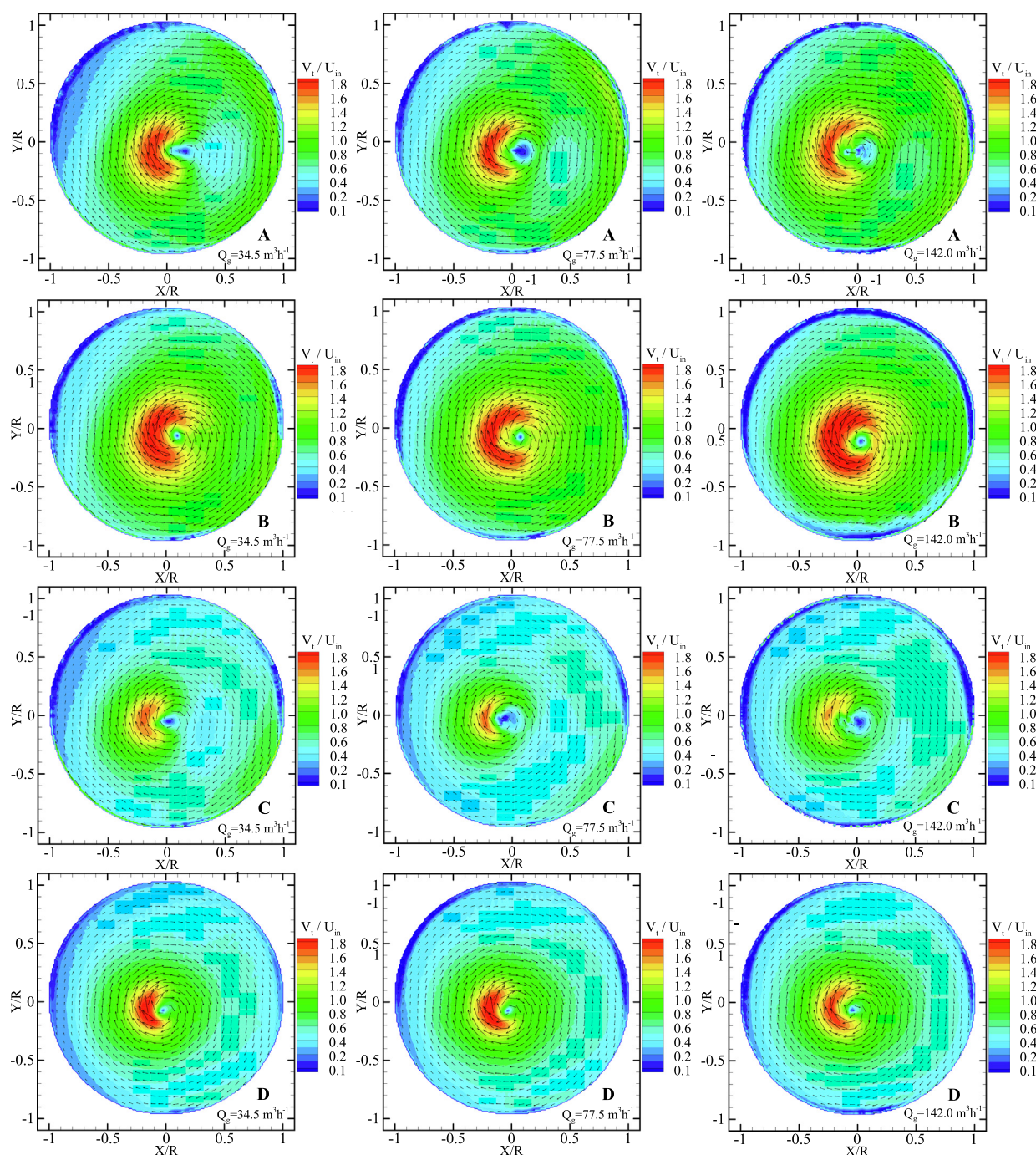

Fig. 7. PIV measured tangential velocity fields $z/l = -0.696$ for all configuration **A** to **D** (from top to bottom) and all gas flow rates 34.5, 77.5 and 142.0 m³h⁻¹ (left to right).
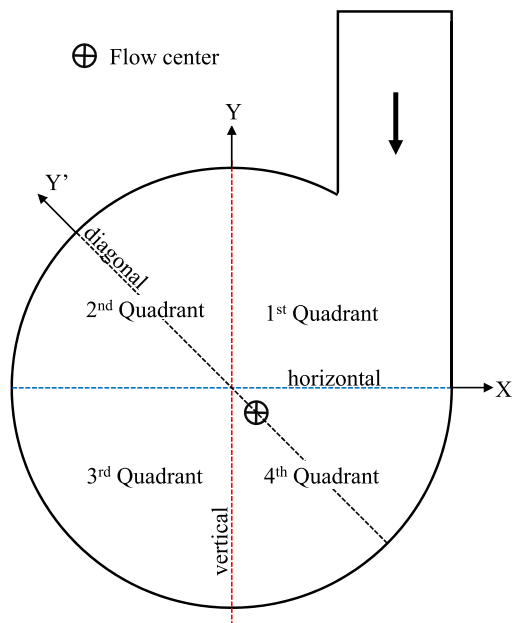
Gustavo E.O. Celis, Juliana B.R. Loureiro, Paulo L.C. Lage et al.

Chemical Engineering Science 248 (2022) 117099

center line, reverse flow is noted, in particular, for the highest gas flow rate.

To further illustrate the above described phenomena, local mean axial velocity profiles are shown in Fig. 6. The data is shown at three z-positions for all configurations and one typical gas flow rate (the intermediate flow rate, Q_g = 77.5 m^{3}h^{-1}). The local profiles consistently illustrate the break in symmetry and show with clarity the influence of the geometry on the flow pattern. It is of interest to note how the levels of the curves on the rhs of Fig. 6 (positive X/R) change positions (from top to bottom and vice versa) as they move to the lhs (negative X/R) and this feature is salient to all geometries.

To evaluate the tangential and radial velocity components of the flow, a pre-requisite is the estimation of the center of rotation. This can be made in two ways: (i) all velocity fields are averaged and the resulting mean field is used to determine the center of rotation (X_c, Y_c), (ii) every instantaneous velocity field has the center of rotation (x_c, y_c) determined and the set of all rotation centers is averaged, $(\bar{x}_c, \bar{y}_c)$. The former option is the simpler, but does not permit to follow the trajectory of (x_c, y_c) and evaluate its precession frequency. The method used for the determination of the center of rotation from given PIV images is detailed in Appendix A. Table 2 shows the results for (X_c, Y_c), which were used to determined the fields of V_t and V_r presented below. The $(\bar{x}_c, \bar{y}_c)$ results and their comparison to (X_c, Y_c) are discussed in Section 4.3.

The absolute tangential velocity (V_t) distributions for the four configurations are shown in Fig. 7. In view of the position of the inlet pipe and the orientation of the coordinate system, the fluid motion is in the clockwise direction (negative V_t). The flow asymmetry already observed for the axial velocity distributions is
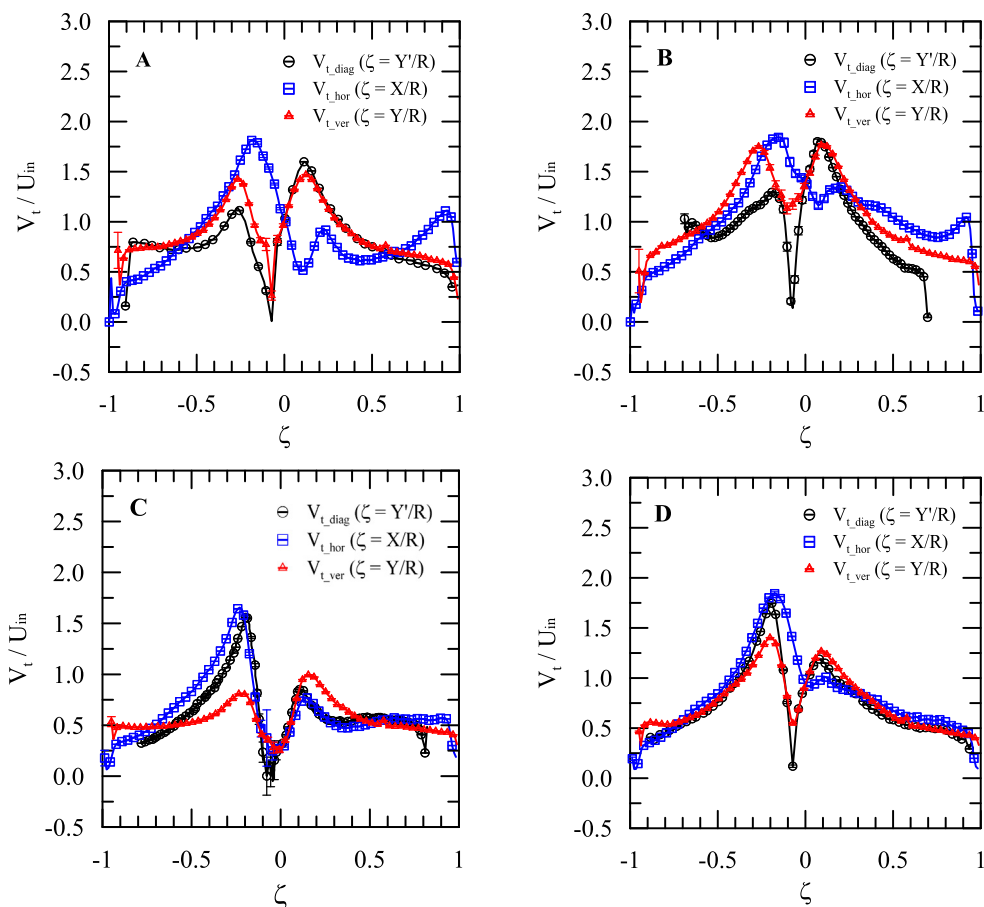

Fig. 8. Coordinate system for the local profiles.

tral region extract fluid more efficiently so that the flow in the nether regions of the cyclone close to the Chinese hat is reduced.

Configuration **D** shows the most symmetric flow pattern, with high velocity twin peaks of about the same values. In the axial

Fig. 9. Local PIV-measured tangential velocity fields for all configuration **A** to **D** and flow rate 77.5 m^{3}h^{-1} at position z/l = -0.696. $\zeta = X/R, Y/R$ or Y'/R is a dummy variable defined according to the reference axes shown in Fig. 8.
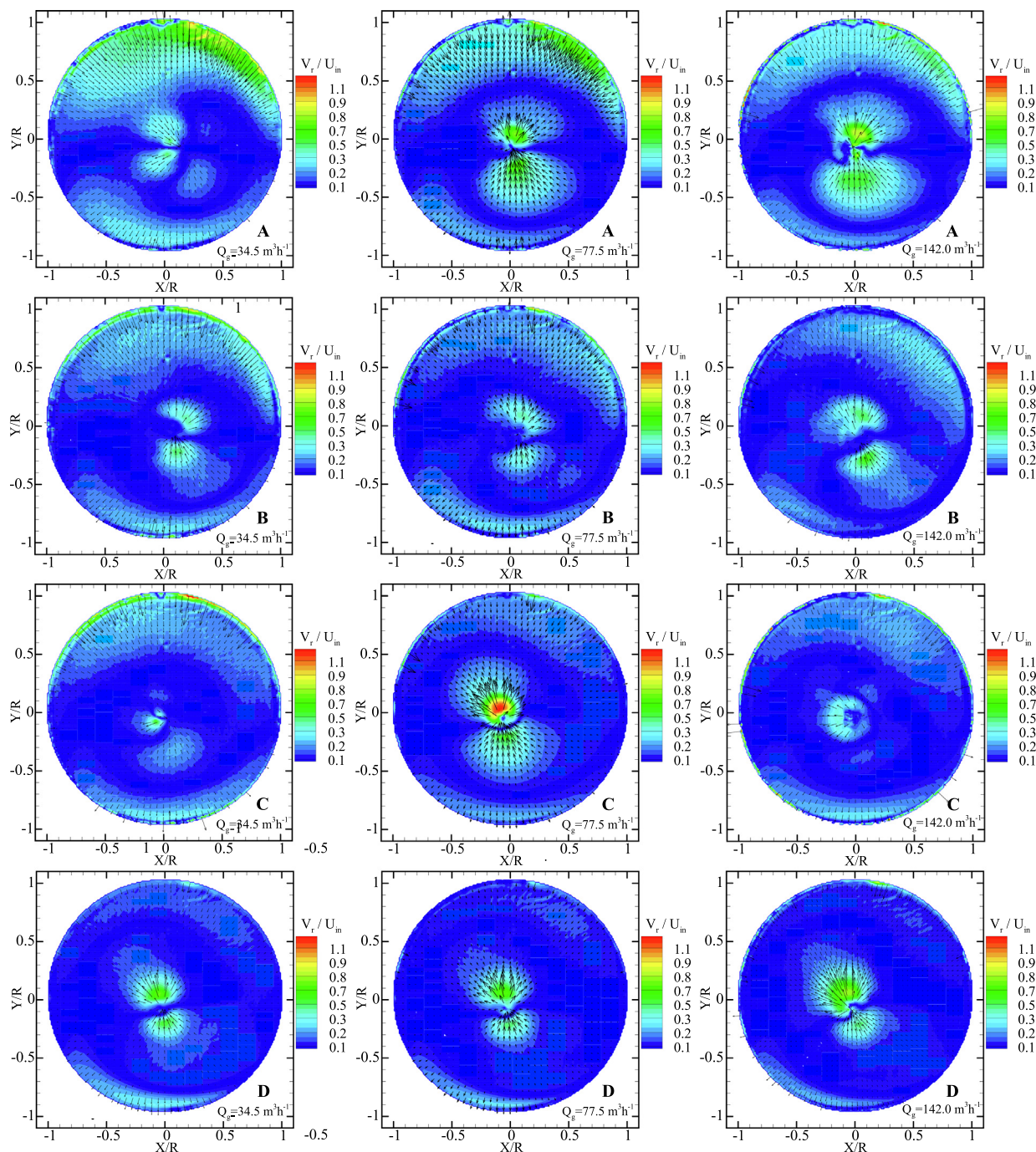
Fig. 10. PIV-measured radial velocity fields z/l = −0.696 for all configuration **A** to **D** (from top to bottom) and all gas flow rates 34.5, 77.5 and 142.0 m³h⁻¹ (left to right).

further observed in the cross section plane as a result of the flow inlet. The more pronounced asymmetry is manifested through axis Y/R. The actual center of rotation is clearly off the geometric center of the cyclone and is characterized by the dark blue regions of circular shape and close to the center of the circumference. For configurations **A** and **B** the center of rotation is offset to the right (positive X/R, Quadrant 4)(Fig. 8). The swirl blades result in a much more organized motion (configurations **C** and **D**), with the rotation center tending to occupy Quadrant 3 in a location close to the geometric center of the cylinder.

The Chinese hat in configurations **B** and **D** clearly tends to retard the flow further away from the central region of the cyclone, with a corresponding increase in V_t in the region near the vertical

symmetry axis. Please, compare configurations **A** to **B** and **C** to **D** (Fig. 7) to observe the relative increase in tangential velocity in the central region of the cyclone (the red zones). The swirl blades have the opposite effect, they tend to establish a more regular velocity distribution with lower peak values. Also, since the swirl blades tend to provoke a more efficient extraction of fluid close to the vortex finder as compared to the other configurations, the tangential velocities at position z/l = −0.696 are lower than in the other configurations.

To show the local data on V_t, the dummy variable ζ is used where $\zeta = X/R, Y/R$ or Y'/R is defined according to the reference axes shown in Fig. 8. These axes are normally used in literature to illustrate the local behavior of V_t, despite the fact that they do
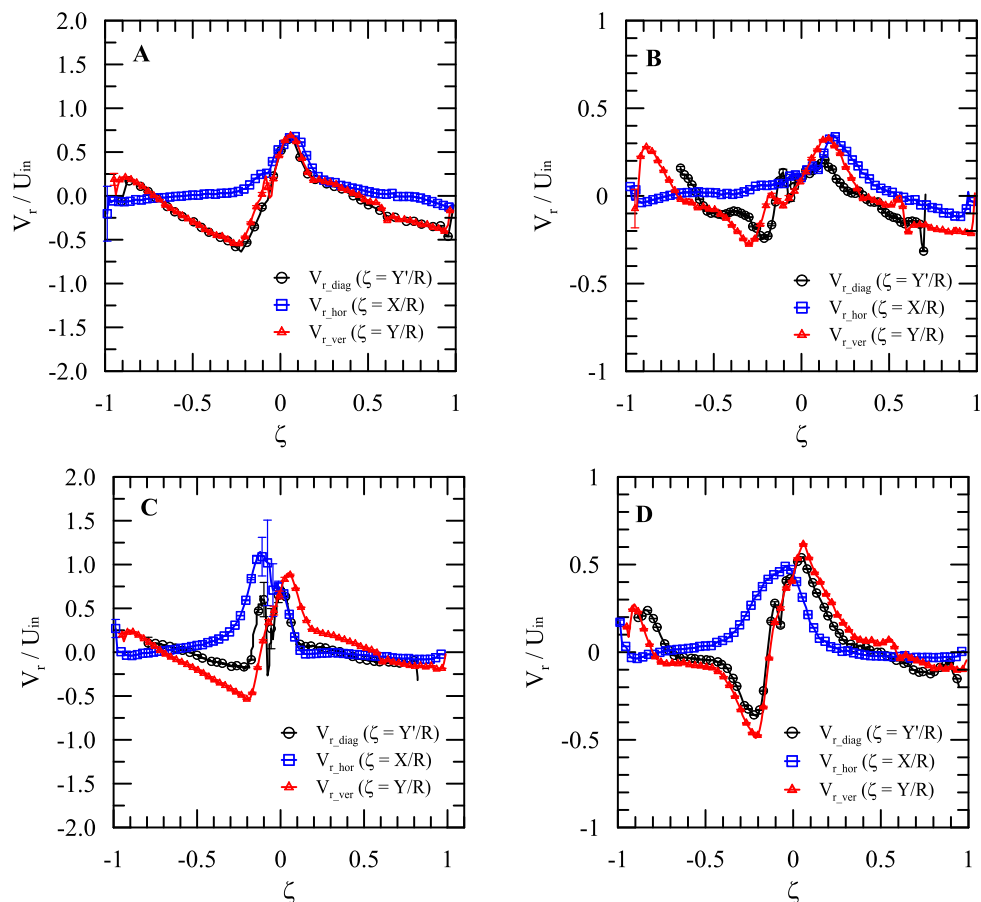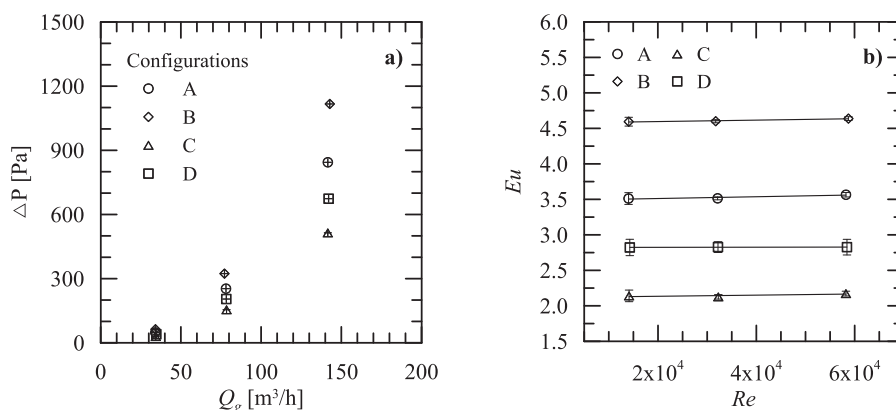
Gustavo E.O. Celis, Juliana B.R. Loureiro, Paulo L.C. Lage et al.

Chemical Engineering Science 248 (2022) 117099

Fig. 11. Local PIV measured radial velocity fields for all configuration **A** to **D** and flow rate 77.5 m³h⁻¹ at position z/l = −0.696. $\zeta = X/R, Y/R$ or Y'/R is a dummy variable defined according to the reference axes shown in Fig. 8.

Fig. 12. a) Dimensional pressure drop, **b)** Euler number.

not coincide with the mean center of rotation of the flow. However, they are convenient in view of their coincidence with the geometric center of the cyclone.

The local absolute values of V_t are shown in Fig. 9. The tangential velocity increases in Quadrants 4 and 3 and subsequently decreases in Quadrant 2 as to return to the values of Quadrant 1. For all configurations, the peak values of V_t/U_{in} are around 2 and about position X/R = −0.2. For configurations **A** and **B**, V_t is very symmetric around the origin of the axis Y/R, with a peak value of 1.5. The swirl blades in the absence of the Chinese hat (configu-

ration **C**) reduce the peak value of V_t/U_{in} to 0.5 at Y/R = −0.2, setting a velocity field relatively symmetric in relation to Y/R, but very asymmetric in relation to X/R and Y'/R.

Despite the off-centered position of the zero tangential velocity, the velocity flow profiles show the existence of a classical Rankine vortex structure in the cyclone, where V_t increases rapidly from zero, reaches a maximum and decreases to zero towards the wall.

The behavior of the radial velocity for all configurations and flow rates is shown in Fig. 10. The dark blue regions are the regions of greatest interest to observe. Since they define positions where V_r

Gustavo E.O. Celis, Juliana B.R. Loureiro, Paulo L.C. Lage et al.

Chemical Engineering Science 248 (2022) 117099

is zero (or close to), they limit regions where the vector velocity components locally converge or diverge defining regions of updraft or downdraft flows. The really striking feature of the V_r-pattern is its strong dependence on the position of the inlet flow and apparent independence on the cyclone configuration. To all configurations, **A** to **D**, and gas flow rates, the top regions of the figures ($Y/R > 0.5$) are dominated by convergent flow (flow in the direction of the geometric center of the separator). The region of divergent flow (toward the wall and down the Chinese hat) is mostly located for ($Y/R < -0.5$).

Differences are clearly noted as figures are compared one to one, but to most figures is it apparent that four simply connected regions exist separated by regions of dark blue color. For configurations **A**, **C** and **D** the regions are easily spotted, two in the central region of the separator, the other two in the top and bottom regions of the figures.

The local profiles of V_r are shown in ζ-coordinate in Fig. 11. The four typical regions of convergent and divergent flows can be characterized by the points where $V_r = 0$. In the (Y/R)-axis (red-triangle symbols), three points of vanishing V_r are observed at approximately $Y/R = 0.5, -0.1, -0.7$. These are approximate values, which however do not change much with the configuration of the separator and the gas flow rates. These points limit the four distinct regions discussed above.

4.2. Pressure drop

For the configurations shown in Fig. 4, and the flow conditions of Table 1, Fig. 12 shows the pressure drop across the cyclonic separator. Fig. 12a shows that ΔP increases almost quadratically with the increase in gas flow rate. This observation is independent of the flow configuration.

The same results are shown in Fig. 12b in dimensionless form in terms of the Euler and Reynolds numbers. The Euler number is defined by $Eu = (2\Delta P)/\left(\rho U_{in}^2\right)$, whereas the Reynolds number is $Re = U_{in}D/\nu$ (U_{in} is the inlet mean velocity). For configuration **A**, $Eu = 3.6$, a value very close to those observed for other separators with a similar geometry (e.g., Karagoz and Avci, 2005 quote $Eu \approx 3.9$).

Configuration **B** provoked the highest value of Eu, a result that may appear counter intuitive due to the absence of the swirl vanes. A common expectation would be that the complete configuration would result in the highest pressure loss due to the combined drag effects of all of the internal elements. The actual picture, however, is different. The swirl blades direct and organize the flow rotation, reducing the pressure losses despite some increase in the friction drag. Thus, configuration **C** results in a much lower pressure loss than configuration **A**. The addition of the Chinese hat to any of

the configurations increases the pressure loss. The Chinese hat stabilizes and accelerates the internal vortex core, which becomes attached to its tip, generating a low-pressure region that extends through the draft tube to the separator outlet and increases the overall pressure loss. To support the above arguments, Fig. 9 shows the large tangential velocities of the inner vortex for configurations **B** and **D** as compared to configurations **A** and **C** respectively. In addition, the CFD simulations (Pereira, 2016) indicate the presence of an extensive low-pressure region when a Chinese hat is present. The implication is that configuration **C** presents the lowest pressure drop (the lowest $Eu = 2.2$). Configuration **D** results in an Eu (= 2.8) which is still very low as compared to configurations **A** and **B** ($Eu = 3.6$ and 4.6 respectively).

The configurations **B** and **C** shown in the work of Nanninga et al. (2001) are comparable to the configurations **B** and **D** of the present work. Here, the reduction of Eu from configuration **B** to **D** is about 37%. In Nanninga et al. (2001), a change from configurations **B** to **C** resulted in a decrease of Eu of about 48%. Despite the differences in the experiments due to the types of flow – single and two-phase – and geometries of the blades, the comparison shows close results.

4.3. Characteristics of the vortex core

A method to determine the position of the axis of rotation of the vortex core from PIV images is described in Appendix A. The average positions of the axis of rotation of the vortex core ($\bar{x}_c, \bar{y}_c$) and the standard deviations (Std) are shown in Table 3. The results suggest that the amplitude of the vortex core motion depends on both the configuration and the flow rate. Since the values of Std are considerably high, it is very difficult to draw any firm conclusion on the effects that changes in the gas flow rate exert on the vortex center position. For most cases, the set ($\bar{x}_c, \bar{y}_c$) agrees well with the corresponding set (X_c, Y_c) shown in Table 2, to within twice of the respective standard deviations. The only exception occurs for condition **A**-$E1$, where a much higher value of X_c (10.8 mm) was observed as compared to the $\bar{x}_c$ value of Table 3. The calculations were double checked and confirmed indeed that this discrepancy stems from the different manners in which the position of the center of rotation is estimated.

The ($\bar{x}_c, \bar{y}_c$) data are also coherent with the observations reported by Hoekstra et al. (1999), for all configurations. These authors also found the measured tangential velocity profiles not to be symmetric in relation to the geometric centreline of the cyclone. Gorton-Hlgerth (apud Obermair et al., 2003) mention that the vortex precession is not around the cyclone axis, but around an axis that spirals around the cyclone axis.

To evaluate the PVC frequency (f_{pvc}) from the low frequency PIV measurements, the statistical method introduced in Appendix A was used. The results for the most probable values of the f_{pvc} and their corresponding errors with a 95% confidence level are shown in Table 4. For the lowest gas flow rate, $E1$ (= 34.5 m^{3}h^{-1}), the effect of the internals on f_{pvc} is very small. For the other two flow conditions, $E2$ and $E3$ (= 77.5 and 142 m^{3}h^{-1}), the Chinese hat seems to damp f_{pvc} resulting in lower values for configurations

Table 4
PVC frequency for the four configurations (**A**, **B**, **C** and **D**) and the three flow conditions (E1, E2 and E3).

Configuration	$f_{pvc}[Hz]$		
	E1	E2	E3
A	265 ± 46	561 ± 85	1958 ± 284
B	270 ± 58	438 ± 45	1117 ± 158
C	288 ± 47	524 ± 101	2283 ± 630
D	302 ± 56	445 ± 69	1028 ± 151

Table 3
Vortex core center position.

Configuration	Flow Condition	$\bar{x}_c$ [mm]	$\bar{y}_c$ [mm]	Std $\bar{x}_c$ [mm]	Std $\bar{y}_c$ [mm]
A	E1	1.5	−6.4	1.9	1.7
	E2	1.1	−6.4	2.4	2.5
	E3	−0.6	−5.9	1.9	2.1
B	E1	6.4	−5.8	1.4	1.4
	E2	4.3	−6.6	1.6	1.6
	E3	1.3	−8.7	2.1	1.9
C	E1	−4.4	−3.9	1.1	1.1
	E2	−5.2	−2.6	1.8	1.7
	E3	−4.5	−3.3	1.9	1.9
D	E1	−2.5	−5.4	0.9	0.8
	E2	−3.0	−5.6	1.4	1.4
	E3	−2.9	−4.3	1.3	1.3

Gustavo E.O. Celis, Juliana B.R. Loureiro, Paulo L.C. Lage et al.

Chemical Engineering Science 248 (2022) 117099

Table 5
Influence of internals on PVC frequency change with flow rate.

Configuration		A	B	C	D
Condition	Q/Q_{E1}	$f_{pvc}/f_{pvc_{E1}}$			
E1	1.00	1.00 ± 0.25	1.00 ± 0.30	1.00 ± 0.23	1.00 ± 0.26
E2	2.25	2.12 ± 0.49	1.62 ± 0.38	1.82 ± 0.46	1.47 ± 0.36
E3	4.12	7.39 ± 1.67	4.13 ± 1.06	7.91 ± 2.53	3.40 ± 0.80
$a \pm \mathrm{Std}\,a$		0.635 ± 0.012	0.442 ± 0.019	0.640 ± 0.049	0.384 ± 0.017

B and **D**. The highest value of f_{pvc} is achieved for configuration **C** and condition $E3$ (= 2283 Hz).

Table 5 compares the PVC frequency ratios for the several flow conditions as referred to condition $E1$ (Q_{E1} denotes the gas flow rate at condition $E1$). The mean errors were obtained by propagating the f_{pvc} errors given in Table 4. It is clear from the data that the increase in the PVC frequency with the flow rate strongly depends on the flow configuration. To quantify this effect, Eq. (3) was adjusted to the data shown in Table 5 through the maximum likelyhood method and the ODR (orthogonal distance regression) package of Boggs et al. (1990):

$$\ln\left[\frac{f_{pvc}}{f_{pvc_{E1}}}\right] = a\left(\frac{Q}{Q_{E1}} - 1\right) \tag{3}$$

The values determined for parameter a and the corresponding standard errors are given in Table 5. The data of Table 5 clearly show that the *Chinese hat* does reduce the increase of the PVC frequency with the increase in flow rate. These results support the claim that this internal element stabilizes the vortex core and that this effect increases with the flow rate.

5. Conclusions

An experimental study on the effects of the internal elements in a specific cyclone separator was successfully presented. PIV and pressure drop data were instrumental to elucidate the role of every element in the flow dynamics. The present measurements are consistent with those of previous authors for confined swirling flow. They highlight the changes in flow symmetry as a result of the cyclone configuration, show that internal blades can be used to organize the flow, reduce pressure losses, attenuate turbulence, stabilize the precession of the vortex core and improve separation.

Swirl vanes have often been used in technology to enhance separation processes but are mostly related to axial separators. The present authors were not very successful in finding extensive literature on phase separators that simultaneously resort to tangential inlet and guiding vanes for process optimization. The contribution of (Zhou et al., 2018) is fairly recent and is one of the few we detected with a content similar to the present study. On the other hand, industrial separators with the configuration **D** discussed here have been extensively used in specific industry niches for over twenty years. This particular configuration has rarely been addressed in literature and one of the main purposes of the present work has been to fill this gap.

The present work introduces a new method to estimate the precession frequency of the vortex core from low-frequency PIV data. The transient aspects of the problem have not been extensively discussed here and are to be addressed elsewhere. In particular, flow fluctuations that are part of the coherent precessing vortex core motion are not part of turbulence (which are rapidly varying fluctuations), meaning that the orderly precessing motion of the core with a specific frequency must be subtracted, along with the average velocity, from the transient velocity signals before any turbulent statistic is calculated. The work of Derksen and collaborators (Derksen and Van den Akker, 2000) uses LES simulations to discuss the effect of the PVC on the levels of the velocity fluctuations, mapping the regions where this influence is more (or less) pronounced.

CRediT authorship contribution statement

Gustavo E.O. Celis: Investigation, Validation, Methodology, Formal analysis, Writing – review & editing. **Juliana B.R. Loureiro:** Methodology, Writing – review & editing, Project administration, Resources. **Paulo L.C. Lage:** Conceptualization, Methodology, Formal analysis, Writing – review & editing. **Atila P. Silva Freire:** Conceptualization, Validation, Writing – original draft, Supervision.

Declaration of Competing Interest

The authors declare that they have no known competing financial interests or personal relationships that could have appeared to influence the work reported in this paper.

Acknowledgements

Appendix A. A vortex core center detection and frequency estimation method on swirling flows from PIV images

The presently proposed method to assess the precessing vortex core (PVC) frequency of a confined swirling flow applies only for low-frequency 2D-PIV measurements. The method is divided into two steps: (i) the identification of the vortex core center position for given pairs of double frame images for the complete data set and (ii) the estimation of the PVC frequency (f_{pvc}). These two steps are discussed below in separate sections.

A.1. Vortex core center detection

Seeding particles on swirling flows rarely reach the center of the vortex core, mainly because of the centrifugal forces and the zero velocity condition at the vortex core center. This creates a particle-lacking area (PLA) that increases as the swirl intensity increases in the flow (Peng et al., 2005).

Fig. A.1, shows a calibrated gray scaled PIV image, where a low (almost zero) particle density region close to the geometric center is observed. This region correspond to the PLA. Since the zero velocity condition of the core flow corresponds to the vortex core center, then, the position of the vortex core center is located in this specific region.

The process to identify the particle-lacking area starts by cutting the central part of the original image into a smaller region
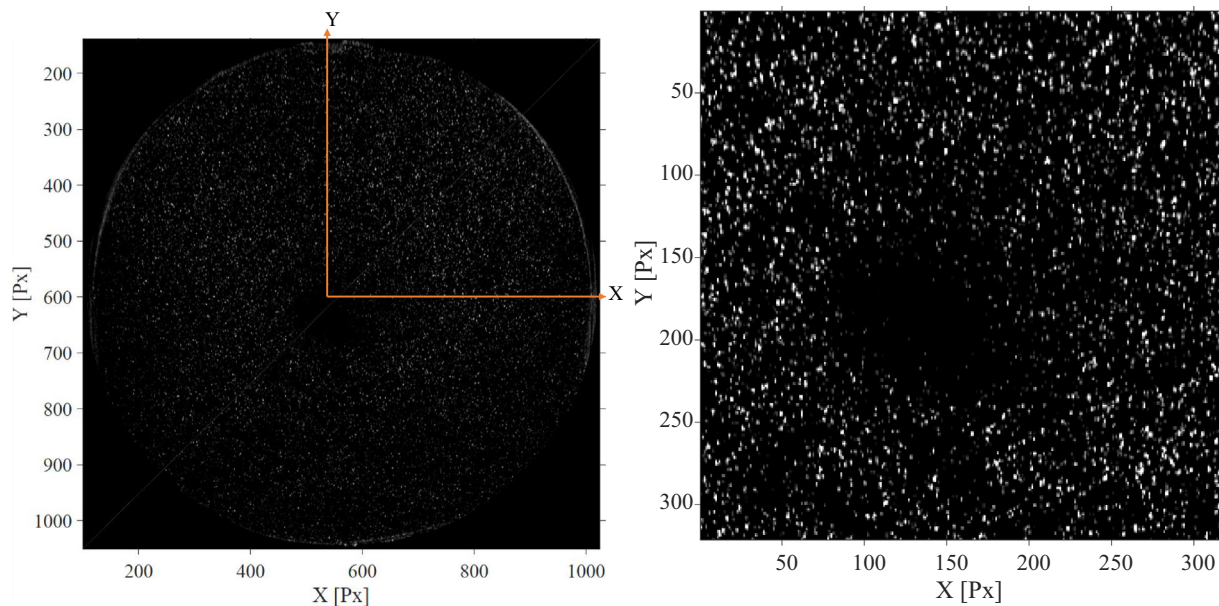
Gustavo E.O. Celis, Juliana B.R. Loureiro, Paulo L.C. Lage et al.

Chemical Engineering Science 248 (2022) 117099

Fig. A.1. Gray scaled and enhanced contrast PIV image. (a) Acquired and calibrated image, (b) Cut and enhanced contrast image.
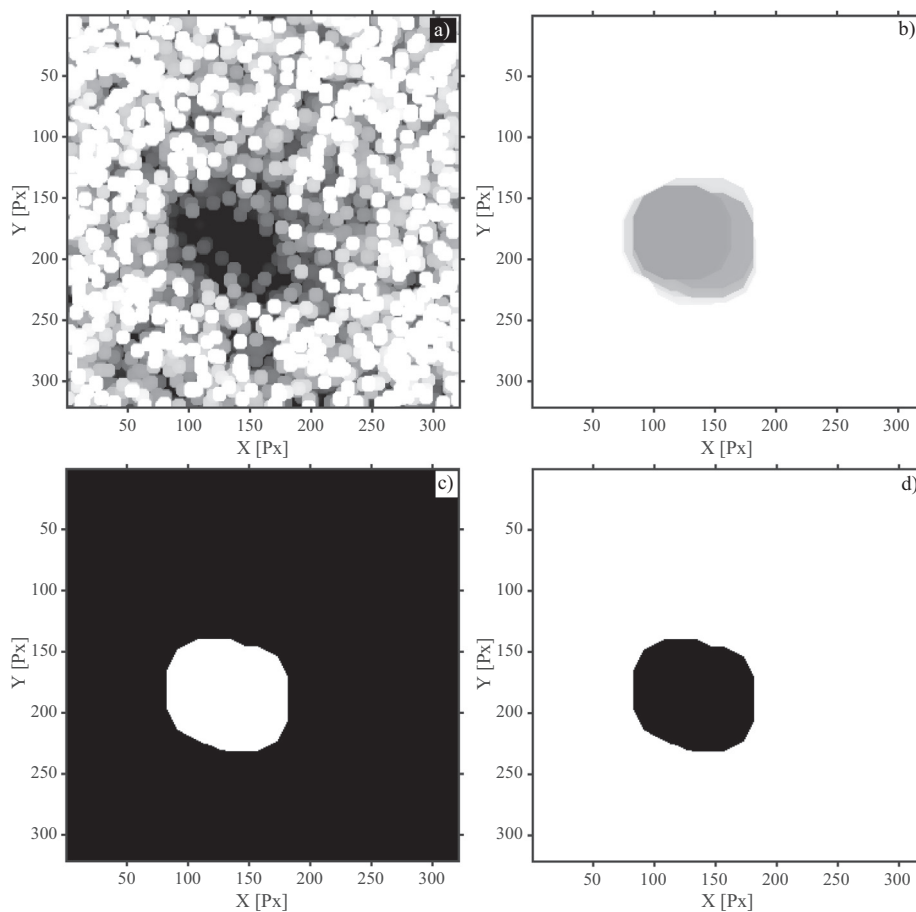

Fig. A.2. Sequential stages in the image process: (a) dilation filter, (b) erosion filter, (c) threshold and noise removal filters, (d) particle-lacking area.

and enhancing its contrast as shown in Fig. A.1. The enhanced contrast is achieved by subtracting from each individual image the mean image. The size of the selected region equals a square matrix of $0.7R \times 0.7R$, where R is the maximum radius of the flow domain, 461 pixels in the present case.

Once a region is selected, a sequence of arithmetic and morphological operations are applied in order to identify the particle-lacking area, as illustrated in Fig. A.2. The first morphological operation is a dilation, where the value of an output pixel is the maximum value of all pixels in its neighborhood (Fig. A.2a). The value of
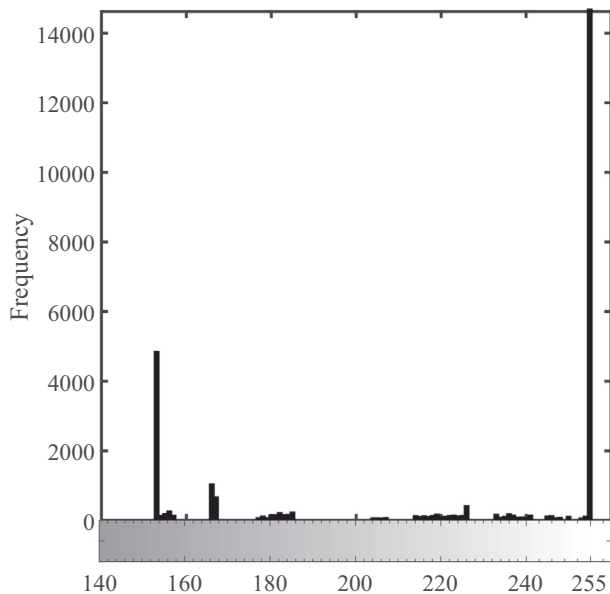
Gustavo E.O. Celis, Juliana B.R. Loureiro, Paulo L.C. Lage et al.

Chemical Engineering Science 248 (2022) 117099

Fig. A.3. Intensity pixel histogram.

an output pixel subject to an erosion operation is the minimum value of all pixels in its neighborhood. This operation removes islands and small objects and keeps only substantive objects (Fig. A.2b). For both operations – dilation and erosion – the state of any given pixel in the output image is determined by the matrix known as "structuring element", which identifies the pixel in the image being processed and defines the neighborhood used in the processing of each pixel. Since the objects that surround the PLA are particles, their shapes are considered spherical and the selected structuring element is a circle. This assumption increases the particle radii without distorting its shape.

Fig. A.2b is still a gray-scaled image, where the boundaries of the PLA are not well defined. A threshold criterion is defined to each frame to obtain the final binary image. The method of Otsu (1979) defines a criterion to determine the local threshold value. The method is based on the zero and the first-order cumulative moments of the gray scaled level histogram to define the optimal threshold value. Fig. A.3 shows the histogram of pixel intensity

with two distinct peaks. From this result, the zero and first order cumulative moments of the gray scaled image can be computed up to a chosen threshold value. Then, the optimization of the separability of the threshold (Otsu, 1979) gives its optimal value. Fig. A.2c shows a binary image following the application Otsu's method. This image is next inverted to reveal the black particle-lacking area (Fig. A.2d).

Since the barycenter of the position of each pixel in Fig. A.2d is known, the instantaneous position of the center of the vortex core may be calculated through the mean geometric value of the PLA, given by Eq. (A.1),

$$x_c = \frac{1}{J}\sum_j x_j, \quad y_c = \frac{1}{J}\sum_j y_j, \tag{A.1}$$

where x_c and y_c stand for the instantaneous position of vortex center in Cartesian reference framework, and (x_j, y_j) is the position of the barycenter of a pixel belonging to the particle-lacking area.

An application of the former processes to every pair of double frame images for the all data set, results in a map that furnishes the instantaneous vortex core center positions (Fig. A.4). In the present study, the vortex core center does not coincide with the geometric center of the separator. Thus, the vortex core does not rotate around the geometric center, but around a displaced axis located at the mean position of the instantaneous vortex core center positions, $\bar{x}_c$ and $\bar{y}_c$ (Fig. A.4). This observed behavior is different from those discussed by other authors (Yazdabadi et al., 1994; Wu and Shi, 2003), who consider the rotation of vortex core around the geometric center of the separator.

A.2. Precessing vortex core frequency

After the determination of the vortex core center time-averaged position, $(\bar{x}_c, \bar{y}_c)$, one can define the following relative position vectors of the instantaneous vortex core position at two sequential time instants (x_{c1}, y_{c1}), (x_{c2}, y_{c2}) as shown in Eq. A.2

$$\mathbf{r_j} = (x_{cj} - \bar{x}_c)\hat{\mathbf{e}}_\mathbf{x} + (y_{cj} - \bar{y}_c)\hat{\mathbf{e}}_\mathbf{y}, \quad r_j = |\mathbf{r_j}|, \quad j = 1,2. \tag{A.2}$$

If the motion between these two time instants is purely rotational, $r_1 = r_2$ as shown in Fig. A.5a, we can compute the angle of rotation β from Eq. (A.3) and the f_{pvc} can be estimated from Eq. (A.4), where t_{pc} is the time between laser pulses.
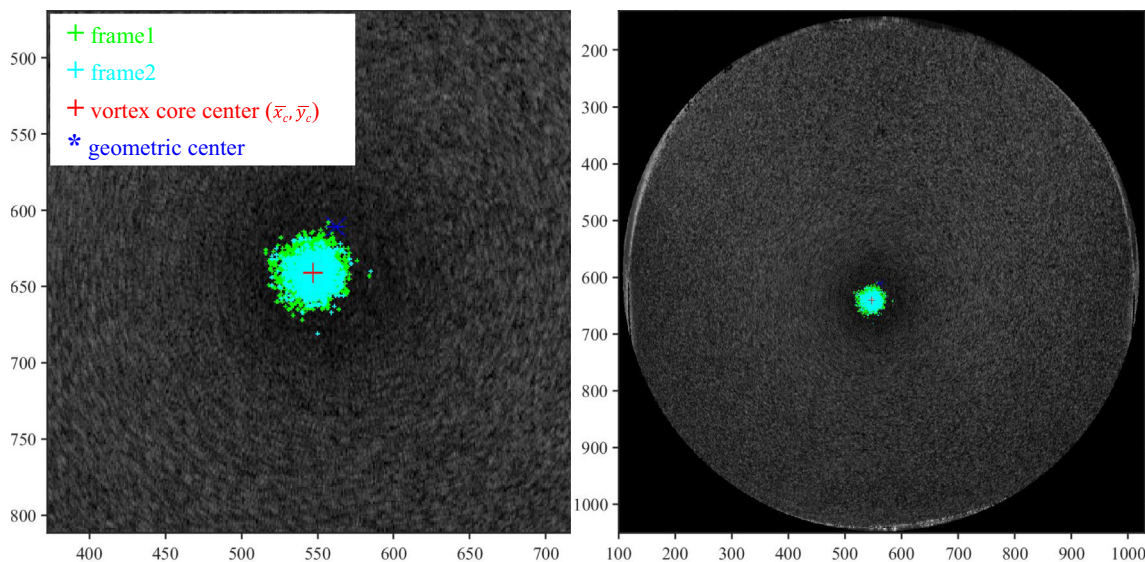
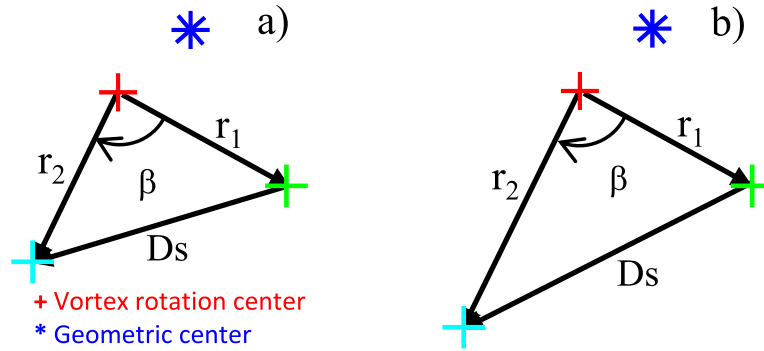

Fig. A.4. Instantaneous vortex core center positions.

Gustavo E.O. Celis, Juliana B.R. Loureiro, Paulo L.C. Lage et al.

Chemical Engineering Science 248 (2022) 117099

Fig. A.5. Instantaneous vortex core center position.

$$\beta = cos^{-1}\left(\frac{\mathbf{r_1} \cdot \mathbf{r_2}}{r_1\ r_2}\right) \quad [rad], \tag{A.3}$$

$$f_{pvc} = \frac{\beta}{2\pi t_{pc}} \quad [Hz]. \tag{A.4}$$

The estimate of f_{pvc} considers the following hypotheses.

- The rotation of vortex core is around the mean position of the instantaneous vortex core center.
- Only motions that are close to pure rotation should be considered to estimate the frequency.
- The motions cannot imply a rotation angle larger than a threshold, β_{tol}, with $\beta_{tol} < \pi$, because, even if $r_1 = r_2$, movements with β close to π can be just rectilinear displacements.

Therefore, some criteria must be defined to select the motions that are mainly rotational. Fig. A.5 illustrates two types of motions: pure rotation (Fig. A.5a) and rotation combined with radial displacement (Fig. A.5b where $r_1 \neq r_2$). Ds is defined as the vortex core center displacement magnitude, given by Eqs. (A.5a) (which can be applied indistinctly for both motion types), whereas Eq. (A.5b). (8b) is strictly valid only for pure rotational motions (Fig. A.5a).

$$Ds = \sqrt{(r_2 - r_1)^2\ \hat{i} + (r_2 - r_1)^2\ \hat{j}}, \tag{A.5a}$$
$$Ds = (r_1 + r_2)sin\left(\frac{\beta}{2}\right). \tag{A.5b}$$
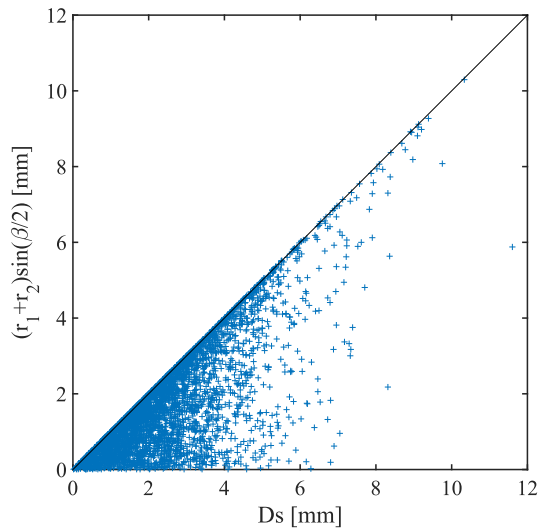
Fig. A.6. Scattering of the displacement behavior related to Ds magnitude.
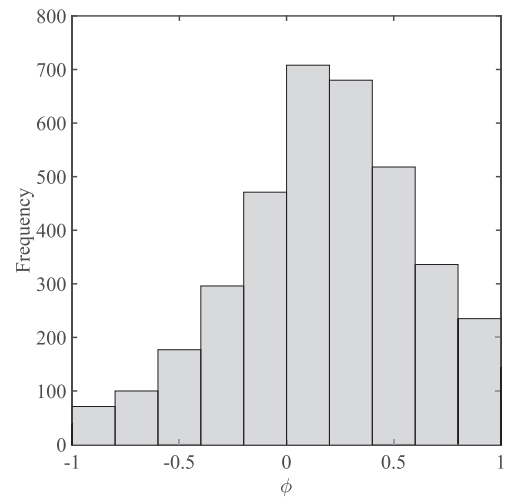
Fig. A.7. Distribution of ϕ.

However, we need to consider movements for which rotation is dominant, but $r_1 \neq r_2$. A new angle β_{pred}, given by Eq. (A.6), is introduced to establish a criterion for the dominance of rotation in the vortex core center motion.

$$\beta_{pred} = sin^{-1}\left(\frac{Ds}{2r_1}\right) + sin^{-1}\left(\frac{Ds}{2r_2}\right) \quad [rad]. \tag{A.6}$$

Eq. A.6 considers that half of the displacement Ds comes from a pure rotation using each one of the two radii. Of course, provided $r_1 = r_2$, β_{pred} and β are equal. For $r_1 \neq r_2$ so that β_{pred} and β exhibit close values, the motion is dominated by rotation.

The analysis is exemplified in the following for the data obtained for configuration **A** and $E1$ flow condition. The Ds magnitude behavior is observed in Fig. A.6. The values close to the reference line (45°) are motions probably dominated by rotations, whereas values far from the reference line suggest radial dominant displacements.

A normalized parameter ϕ is defined by Eq. (A.7), whose values are close to zero when the vortex core center displacement is dominated by rotation, that is, $r_1 \approx r_2$.

$$\phi = 2\left(\frac{r_1 - r_2}{r_1 + r_2}\right). \tag{A.7}$$

A histogram of ϕ shows that the motions dominated by rotations are prevalent, as the maximum relative frequency of all movements occurs nearby $\phi = 0$ (see Figure A.7).
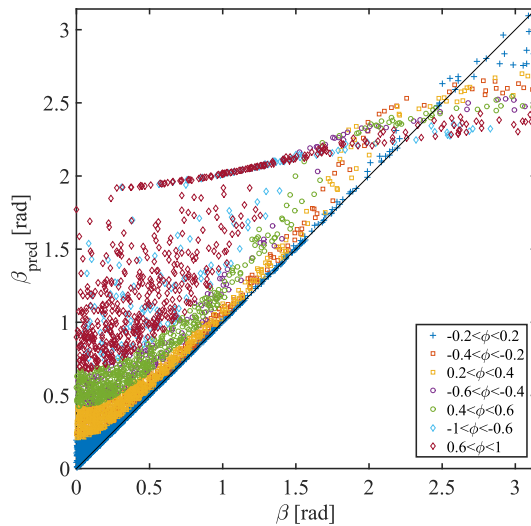
Gustavo E.O. Celis, Juliana B.R. Loureiro, Paulo L.C. Lage et al.

Chemical Engineering Science 248 (2022) 117099

Fig. A.8. Comparison between β and β_{pred}.
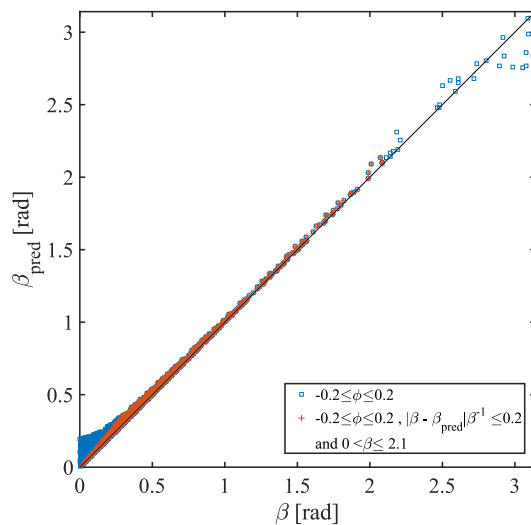

Fig. A.9. Application of the criteria to select the motions dominated by rotation.
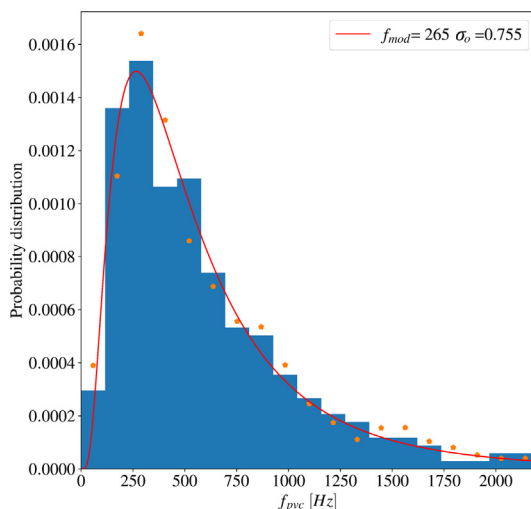

Fig. A.10. PVC frequency histogram.

To define a criterion for the selection of motions dominated by rotation, consider motions that simultaneously satisfy $\beta < \beta_{tol}, |\phi| < \phi_{tol}$ and $PD < PD_{tol}$, where PD is defined by:

$$PD = |\beta - \beta_{pred}| \; \beta^{-1}. \tag{A.8}$$

Fig. A.8 shows the behavior between β and β_{pred} for subgroups with different ϕ values and for $\beta < \pi$. It is clearly seen that motions with $-0.2 < \phi < 0.2$, in general, have β_{pred} close to β. Fig. A.8 also shows that the motions with $|\phi| < 0.2$ are more scattered around the line $\beta = \beta_{pred}$ for $\beta > 2.5$. These motions are discarded by considering $\beta_{tol} = 2.1$ (120 degrees).

Fig. A.9 shows the results obtained after the application of the criterion where the conditions $|\phi| < 0.2, PD < 0.2$ and $\beta < 2.1$ are simultaneously satisfied. It is clear that the proposed criterion selects a subgroup of motions that are probably dominated by rotation.

Once a subgroup of all motions is defined by the proposed criterion, the parameter f_{pvc} can be evaluated using Eq. (A.4) for each motion. Thus, the PVC frequency histogram can be built as shown in Fig. A.10 for configuration **A** and $E1$ flow condition.

To determine the most probable frequency of the PVC distribution, that is, its mode, the log-normal distribution, given by Eq. (A.9), was selected to fit the data. Note that Eq. (A.9) is written using the mode (f_{mod}) and standard deviation (σ_o) as parameters because we were interested in assessing the uncertainty of f_{mod} in the data fit. The estimated values for σ_o and f_{mod} were calculated by using the maximum likelyhood method and the ODR routine (Boggs et al., 1990) to fit Eq. (A.9) to the histogram data. The selected dominant rotation movements were separated into three subgroups to compute the standard deviations of the relative frequencies in the PVC histogram. The variation coefficient of the mode ($CV_{mod} = Std f_{mod}/f_{mod}$) obtained in the fitting procedure was used to define the better choice of histogram parameters (the frequency range and number of bins) for each configuration and flow conditions. The lowest possible value of CV_{mod} defines the best choice of these histogram parameters.

$$G(f) = \frac{1}{f\sigma_o\sqrt{2\pi}} \exp\left[-\frac{(\ln(f) - \mu)^2}{2\sigma_o^2} \right], \quad \mu = \ln(f_{mod}) + \sigma_o^2. \tag{A.9}$$

The error of f_{mod} with a 95% confidence level was estimated using t-Student's distribution and the degrees of freedom of the corresponding histogram data.

References

Austrheim, T., Gjertsen, L.H., Hoffmann, A.C., 2008. An experimental investigation of scrubber internals at conditions of low pressure. Chem. Eng. J. 138 (1–3), 95–102. https://doi.org/10.1016/j.cej.2007.05.048.

Bandyopadhyay, P.R., Gad-el Hak, M., 1996. Rotating gas-liquid flows in finite cylinders: Sensitivity of standing vortices to end effects. Exp. in Fluids 21, 124–138. https://doi.org/10.1007/BF00193916.

Bergström, J., Vomhoff, H., 2007. Experimental hydrocyclone flow field studies. Sep. Purif. Technol. 53 (1), 8–20. https://doi.org/10.1016/j.seppur.2006.09.019.

Boggs, P.T., Rogers, J.E., 1990. Statistical analysis of measurement error models and applications. In: Proceedings of the AMS-IMS-SIAM Joint Summer Research Conference, Vol. 112 of Contemporary Mathematics, American Mathematical Society, doi:10.1090/conm/112.

Brennen, C.E., 2005. Fundamentals of Multiphase Flow. Cambridge University Press. https://doi.org/10.1017/CBO9780511807169.

Derksen, J.J., 2005. Simulations of confined turbulent vortex flow. Comput. Fluids 34, 301–318.

Derksen, J.J., Van den Akker, H.E.A., 2000. Simulation of vortex core precession in a reverse-flow cyclone. AIChE J. 46 (7), 1317. https://doi.org/10.1002/aic.690460706.

Gupta, A.K., Lilley, D.G., Syred, N., 1984. Swirling Flows. Abacus Press, UK. https://doi.org/10.1016/0010-2180(86)90133-1.

Hoekstra, A., Derksen, J., Van den Akker, H., 1999. An experimental and numerical study of turbulent swirling flow in gas cyclones. Chem. Eng. Sci. 54 (13–14), 2055–2065. https://doi.org/10.1016/S0009-2509(98)00373-X.

Gustavo E.O. Celis, Juliana B.R. Loureiro, Paulo L.C. Lage et al.

Chemical Engineering Science 248 (2022) 117099

Hoekstra, A.J., Derksen, J.J., Van den Akker, H.E.A., 1999. An experimental and numerical study of turbulent swirling flow in gas cyclones. Chem. Eng. Sci. 54 (23), 2055–2065. https://doi.org/10.1016/S0009-2509(98)00373-X.

Hoffmann, A.C., Stein, L.E., 2008. Gas cyclones and swirl tubes: Principles, design and operation, vol. 1, Springer, Berlin, Heidelberg, doi:10.1007/978-3-540-74696-6.

Hoffmann, A.C., De Groot, M., Hospers, A., 1996. The effect of the dust collection system on the flow pattern and separation fficiency of a gas cyclone. Can. J. Chem. Eng. 74 (4), 464–470. https://doi.org/10.1002/cjce.5450740405.

Hreiz, R., Gentric, C., Midoux, N., 2011. Numerical investigation of swirling flow in cylindrical cyclones. Chem. Eng. Res. Des. (8), 2521–2539

Janssen, J.W.F., Betting, M., 2006. Combined Test with the Improved Performance Twister Supersonic Separator and the Gasunie Cyclone Separator. In: 23rd World Gas Conference, pp. 1–15.

Karagoz, I., Avci, A., 2005. Modelling of the pressure drop in tangential inlet cyclone separators. Aerosol Sci. Technol. 39 (9), 857–865. https://doi.org/10.1080/02786820500295560.

Kremleva, E., Fantoft, R., Mikelsen, R., Akdim, R., 2010. Inline technologynew solutions for gas/liquid separation. SPE Russian Petroleum Technology Conference. Paper Number: SPE-136390-MS, doi:10.2118/136390-MS.

Li, Q., Xu, W., Wang, J., Jin, Y., 2015. Performance evaluation of a new cyclone separator Part I experimental results. Sep. Purif. Technol. 141, 53–58. https://doi.org/10.1016/j.seppur.2014.10.030.

Liu, Z., Jiao, J., Zheng, Y., 2006. Study of axial velocity in gas cyclones by 2D-PIV, 3D-PIV, and simulation. China Particuol. 4 (3–4), 204–210. https://doi.org/10.1016/S1672-2515(07)60262-0.

Liu, Z., Zheng, Y., Jia, L., Zhang, Q., 2007. An experimental method of examining three-dimensional swirling flows in gas cyclones by 2D-PIV. Chem. Eng. J. 133 (1–3), 247–256. https://doi.org/10.1016/j.cej.2007.02.015.

Misiulia, D., Andersson, A.G., Lundstrom, T.S., 2015. Effects of the inlet angles on the flow pattern and pressure drop of a cyclone with helical-roof inlet. Chem. Eng. Res. Des. 102, 307–321. https://doi.org/10.1016/j.cherd.2015.06.036.

Monredon, T.C., Hsieh, K.T., Rajamani, R.K., 1992. Fluid flow model of the hydrocyclone: an investigation of device dimensions. Int. J. Miner. Process. 35 (1–2), 65–83. https://doi.org/10.1016/0301-7516(92)90005-H.

Nanninga, N., Janssen, J., Van Asperen, V., 2001. Gasunie/CDS improvement of the gasunie cyclone gas-liquid separator. In: International Gas Research Conference Proceedings.

Obermair, S., Woisetschläger, J., Staudinger, G., 2003. Investigation of the flow pattern in different dust outlet geometries of a gas cyclone by laser doppler anemometry. Powder Technol. 138 (2–3), 239–251. https://doi.org/10.1016/j.powtec.2003.09.009.

Otsu, N., 1979. A threshold selection method from gray-level histograms. IEEE Trans. Syst. Man Cybernet. 9 (1), 62–66. https://doi.org/10.1109/TSMC.1979.4310076.

Peng, W., Boot, P.J.A.J., Hoffmann, A.C., Dries, H.W.A., Kater, J., Ekker, A., 2001. Flow in the inlet region in tangential inlet cyclones. Ind. Eng. Chem. Res. 40 (23), 5649–5655. https://doi.org/10.1021/ie010226q.

Peng, W., Hoffmann, A.C., Dries, H.W.A., Regelink, M., Foo, K.-K., 2005. Neutrally buoyant tracer in gas cleaning equipment: a case study. Measur. Sci. Technol. 16 (12), 2405–2414. https://doi.org/10.1088/0957-0233/16/12/002.

Pereira, M.G., 2016. Numerical simulation of a gas-liquid cyclonic separator with internal parts (in Portuguese), Master's thesis, Chemical Engineering Program, COPPE/UFRJ.

Qian, F., Zhang, M., 2007. Effects of the inlet section angle on the flow field of a cyclone. Chem. Eng. Technol. 30 (11), 1564–1570. https://doi.org/10.1002/ceat.200700246.

Sahovic, B., Atmani, H., Sattar, M.A., Garcia, M.M., Schleicher, E., Legendre, D., Climent, E., Zamansky, R., Pedrono, A., Babout, L., Banasiak, R., Portela, L.M., Hampel, U., 2020. A Numerical and Experimental Survey of a Liquid-Liquid Axial Cyclone. Chem. Ing. Tech. 92 (5), 554–563.

Smith, J.L., 1962. An experimental study of the vortex in the cyclone separator. J. Basic Eng. 84, 602–608. https://doi.org/10.1115/1.3658721.

Syred, N., 2006. A review of oscillation mechanisms and the role of the precessing vortex core (PVC) in swirl combustion systems. Prog. Energy Combust. Sci. 32 (2), 93–161. https://doi.org/10.1016/j.pecs.2005.10.002.

Ter Linden, A.J., 1949. Investigations into cyclone dust collectors. In: Proceedings of the Institution of Mechanical Engineers, Vol. 160, pp. 233–251. doi:10.1243/PIME_PROC_1949_160_025_02.

van Campen, L., Muddey, R.F., Slotz, J., Hoeijmaker, H., 2012. A Numerical and Experimental Survey of a Liquid-Liquid Axial Cyclone. Int. J. Chem. Reactor Eng. 10 (A35), 1–17.

Wu, X.L., Shi, M.X., 2003. Visualization of the precessing vortex core in a cyclone separator by PIV. Chin. J. Chem. Eng. 11 (6), 633–637. URL http://www.cjche.com.cn/EN/volumn/volumn_1182.shtml#1.

Yazdabadi, P.A., Griffiths, A.J., Syred, N., 1994. Characterization of the PVC phenomena in the exhaust of a cyclone dust separator. Exp. Fluids 17 (1–2), 84–95. https://doi.org/10.1007/BF02412807.

Zhou, F., Sun, G., Han, X., Zhang, Y., Bi, W., 2018. Experimental and CFD study on effects of spiral guide vanes on cyclone performance. Adv. Powder Technol. 29, 3394–3403.